J. Fluid Mech. (2022), *vol.* 938, A4, doi:10.1017/jfm.2022.124

Jet impingement on the underside of a superhydrophobic surface

Roberto M. de la Cruz[1,2] **and Simo A. Mäkiharju**[1,†]

[1]Department of Mechanical Engineering, University of California, Berkeley, CA 94720, USA

[2]Faculty of Aerospace Engineering, TU Delft, Delft, 2629 HS, Netherlands

(Received 18 March 2021; revised 27 January 2022; accepted 3 February 2022)

Water patch topology and momentum loss resulting from a jet impacting on the underside of a flat plate with varied hydrophobicity were studied. The jet's Reynolds and Froude numbers ranged from 3700 to 31 000, and from 1 to 23, respectively. Hence effects of gravity were expected to be non-negligible, and data suggest that this is the case for hydrophobic surfaces. The interplay of gravity, surface tension, inertia and viscosity resulted in two distinct behaviours. On hydrophilic surfaces, water spread uniformly. Friction reduced momentum, and led to accumulation at the edges of the patch until gravity overcame surface tension and produced droplets. On hydrophobic surfaces, two rims formed, enclosing a thin laminar film. The patch shape was mostly determined by the balance of kinetic and surface energy. Dewetting occurred in most cases when the two rims merged, but for a narrow parameter, range water detached soon after impact and formed a type of skewed water bell. The transition in detachment topology was predicted reasonably by a simple model considering whether an attached or detached rim minimizes energy. Due to promotion of dewetting by gravity, the water patch area decreased compared to that reported in previous studies, which considered jet impingement on vertical surfaces and tops of horizontal surfaces. Owing to the application that motivated this study, the streamwise force on the plate was also measured. On hydrophobic surfaces the reduction in force correlated with the reduction in water patch area. Water patch area and momentum loss were both found to scale best with the contact-angle-modified Weber number.

Key words: gas/liquid flow, thin films, drag reduction

1. Introduction

Water impacting on the underside of surfaces has relevance to a range of applications, from surface cleaning and cooling, to air layer drag reduction (Peifer, Callahan-Dudley

† Email address for correspondence: makiharju@berkeley.edu

© The Author(s), 2022. Published by Cambridge University Press. This is an Open Access article, distributed under the terms of the Creative Commons Attribution licence (https://creativecommons.org/licenses/by/4.0/), which permits unrestricted re-use, distribution, and reproduction in any medium, provided the original work is properly cited.

https://doi.org/10.1017/jfm.2022.124 Published online by Cambridge University Press

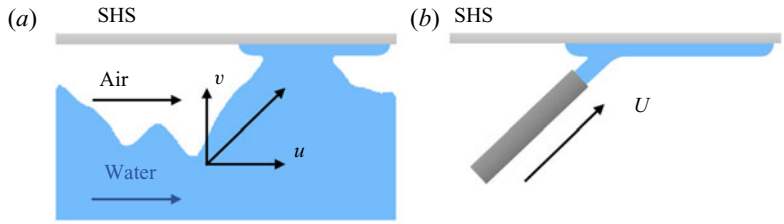

Figure 1. (*a*) Conceptual representation of the wetting event of Peifer *et al.* (2020), with a slug of water rising up through the air layer and impacting the superhydrophobic surface (SHS). (*b*) The simplified repeatable experiment with a jet at an oblique angle impinging on the underside of a flat plate. Here, v, u and U are the vertical, horizontal and scalar water jet velocities, respectively. Gravity acts downwards, normal to the surface.

& Mäkiharju 2020). The latter application was the primary motivation for this study, and necessitated understanding the spread of water upon impingement on the underside of surfaces with varying contact angles and roughness.

In air layer drag reduction, gas is injected underneath the ship's hull, establishing a thin (nominally continuous) layer of air between the ship's hull and the water (Sanders *et al.* 2006; Ceccio 2010; Elbing *et al.* 2013; Mäkiharju *et al.* 2017; Mäkiharju & Ceccio 2018). The resulting frictional drag reduction has already enabled net energy savings up to $O(10\,\%)$, as predicted in Mäkiharju, Perlin & Ceccio (2012). However, if the gas flux requirements could be reduced, then the net energy savings could be more than doubled. This would require a thinner layer of gas to be able to resist breakup. The Kelvin–Helmholtz instability (Kim & Moin 2010) or other omnipresent perturbations of the air–water interface cause the water to frequently attempt to wet the surface and initiate a sequence of events breaking the layer of gas into a bubbly flow that no longer yields the desired reduction in frictional drag.

Peifer *et al.* (2020) and Callahan-Dudley *et al.* (2020) studied whether a hydrophobic surface would promote healing of the continuous air layer, and initial results from these studies indicate that a decrease in air flux by a factor of two or three may still sustain a continuous air layer, if the underlying solid surface is superhydrophobic. However, the relevant physical mechanisms and scaling as a function of surface and flow properties are not yet well understood. As seen in data of Callahan-Dudley *et al.* (2020), following events of water rising and impacting the lower surface of the hull, and multiple such events merging, the continuous air film breaks up. In an attempt to simplify the full problem and to gain better understanding of the effects of the key parameters, it was decided to study isolated wetting events in a reproducible and controlled manner. In this simplified case, the slug of water that contacts the surface through the air layer is replaced by an upward inclined jet, and the ship's hull is represented by a flat plate with varied hydrophobic and roughness properties. The upward inclined jet is thought to mimic the types of oblique impacts that occur through the actual air layer, as depicted in figure 1.

The impact of a jet on a flat plate has received a fair amount of attention, including studies of hydraulic jumps resulting from normal impacts by e.g. Watson (1964), Bhagat *et al.* (2018), Duchesne, Andersen & Bohr (2019) and Bhagat & Linden (2020). Most recently, Moitra *et al.* (2021) also considered impact on a superhydrophobic mesh, and reported hydraulic jumps and Cassie–Baxter to Wenzel transitions. However, no study examined jets impacting the underside of a surface in the parameter range of interest, where both surface properties and orientation with respect to gravity are expected to be significant. Yet much can be learned from the previous results. On hydrophilic surfaces, Kate, Das & Chakraborty (2007) studied – experimentally and theoretically – oblique jets

https://doi.org/10.1017/jfm.2022.124 Published online by Cambridge University Press

impinging on the top of a horizontal surface. This resulted in a hydraulic jump, and the authors derived an expression for its radial location. Wang *et al.* (2013) considered an oblique jet impact on a vertical surface over a parameter range partly overlapping ours, which offers an interesting dataset for comparison considering the effects of gravity.

Kibar *et al.* (2010) showed how surface properties can affect the topology resulting from an oblique jet impinging on a vertical surface. This was studied further numerically by Kibar (2015), who presented an energy argument on the water patch topology that builds on the experimental work of Kaps *et al.* (2014). Similarly, Prince, Maynes & Crockett (2015) also showed that water patch topology resulting from an impinging jet can clearly be influenced by surface hydrophobicity.

Impingement of water microjets on a hydrophobic surface was studied by Celestini *et al.* (2010), who reported mirror rebounds and jumps of 'crawling water'. While concerned only with jets smaller than 1 mm, this work further showed that surface characteristics can have a significant effect on the topology resulting from jet impingement on a surface.

Much work has also been done on two jets impacting in midair, such as the very thoughtful experimental and theoretical study of Bush & Hasha (2004), who found the Rayleigh–Plateau instability of the rims to be responsible for the 'fishbone' topology and ejection of droplets. Their jet's post-impact shape bears a striking similarity qualitatively to the topology observed in the present work. And their conservation-law-based derivation rim-film flow is relevant, albeit justifiably conducted whilst neglecting gravity, given that their Froude number range was one to two orders of magnitude higher than that in the present study.

We undertook this study, as no prior research was found on a jet impacting on the underside of a plate when the parameter range was such that gravity, surface tension, inertia and viscosity all were expected to potentially play a role in water spread and dewetting. Specifically, considering the wetted spot sizes observed in the air layer drag reduction experiments by Peifer *et al.* (2020) and Callahan-Dudley *et al.* (2020), we consider Bond numbers of $O(10)$ and Froude numbers from 1 to 23. Hence gravity effects are presumed to be potentially non-negligible.

This paper is organized as follows. The experimental set-up is described in § 2. Results on hydraulically smooth and rough surfaces are presented and analysed in §§ 3 and 5, respectively. Section 4 compares present findings to those reported by previous investigators to examine gravity's effect, and conclusions are presented in § 6.

2. Experimental set-up

The experimental set-up was designed to enable quantitative image-based measurements of the water patch topology as well as the measurement of the horizontal force exerted on the plate by the jet. The set-up, shown in figure 2, consisted of a plate (horizontal within $<0.4^\circ$) and a brass pipe under the surface from which the jet originated. The pipe's upper edge was 1–3 mm below the plate (3–10 mm to the centre of the jet, depending on the pipe diameter), which was as close as it could be placed without its presence influencing the flow topology. (For closer spacing, the pipe could be observed to interact with the backwards flow from the stagnation point.) The loss in potential energy compared to the jet's kinetic energy due to vertical separation was always less than 12 %, and below 4 % for 92 % of the cases. In the few cases with higher potential energy loss (lowest jet velocity), the impact was partial, as can be seen in panels (a4) and (a5) of figure 4, but these data are included as they were of interest given the motivating application.

https://doi.org/10.1017/jfm.2022.124 Published online by Cambridge University Press

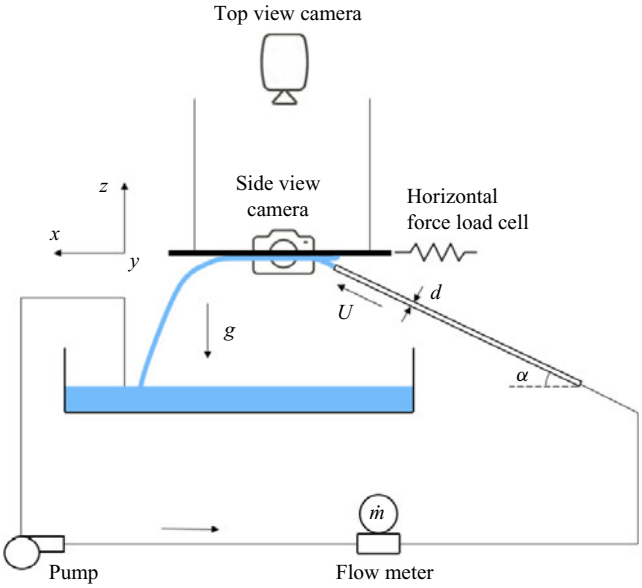

Figure 2. The ascending jet impact set-up. The y-axis on the coordinate system points 'out' of the paper to form a right-handed coordinate system. The parameters $U(=4\dot{m}/\rho\pi d^2)$, d, α, g, ρ and $\dot{m}$ represent the average jet velocity, pipe diameter, initial jet angle, gravitational acceleration, water density and mass flow rate, respectively.

Two cameras were used to record top and side views of the water patch. The top view camera (Basler ace acA2040-55um) was located above the plate looking down through the transparent test surface. (The transparency of the coatings and plate is discussed further in § 2.3.) The side view was captured by a Vision Research Phantom v1210 recording at 100 fps, with 1280 × 800 pixel resolution. A Neewer SL-200W light was used for backlighting. Both cameras were synchronized with force and flow rate measurements.

The water patch area was computed by fitting an ellipse to an average of all images recorded during the experiment, utilizing two different algorithms: (i) using a Hough transform; (ii) defining an ellipse with major and minor axes that correspond to the maximum length and width of the water patch, respectively. If the values from the two measurements were within 2 %, then the value from method (ii) was used. If the values yielded by the two automated algorithms differed more than this, then the ellipse length and width were obtained manually from the images. As an additional check, for all cases, the images of the computed ellipses superimposed on the patch boundaries were inspected visually to ensure that the algorithm had not produced spurious results.

The horizontal (x-component) force on the plate due to the impinging jet was measured utilizing a 100 g load cell connected to a DMD4059 Omega Strain Gauge DC Isolated Transmitter, which acted both as a load cell amplifier and a noise filter. The force measurement was found to agree with calibration weights and be repeatable within 0.5 mN. The plate was suspended from four 1.2 m long wires (Stren SHIQS10-HG High Impact Monofilament) such that any horizontal force imparted by the plate mounting could be assumed negligible.

The flow loop consisted of a 300 l water tank, pump, 30 μm filter, Coriolis flow meter, 19 and 9.5 mm (nominal 3/4″ and 3/8″) inside-diameter tubing, and finally a brass pipe (of varied diameter) from which the jet exited. The water tank collected the liquid falling

https://doi.org/10.1017/jfm.2022.124 Published online by Cambridge University Press

Surface ID	Coating	Contact angle (deg.)	R_a (nm)	k^+
A1	Glass	45 ± 8	12 ± 0.5	<0.0043
A2	NeverWet	101 ± 3	11 ± 0	<0.0081
A4	NaisolSHBC	142 ± 4	1930 ± 40	<2.03
A5	Cytonix800M	150 ± 2	120 ± 6	<0.43
B1	Smooth	78 ± 4	510 ± 263	0.1–0.27
B3	Rough	88 ± 5	$(21 \pm 8) \times 10^3$	4.8–24.6

Table 1. Surface properties, where $\pm$ indicates one standard deviation of the measurements, and R_a and k^+ are the arithmetic mean and dimensionless roughness, respectively.

from the plate. The pump used was a 0.5 hp Goulds MCS 1MS1C5E4 pump controlled by an EATON mmx11aa2d8n0-0 variable frequency drive, which enabled a repeatable flow within the accuracy of the mass flow measurement. The mass flow rate was measured with a Micromotion CMF025M319N0AMEZZZ-2400S Coriolis flow meter, which additionally yielded a water temperature measurement. This flow meter has a manufacturer-specified uncertainty of 0.05 % of reading. (The flow meter performance was also verified by comparing readings against measurement of the mass of water accumulated in a secondary reservoir over a period of two minutes. Data were found to agree within the measurement uncertainty.)

The pipes (of varied diameters) from which the jet emerged were all 0.9 m long, ($>15\times$ the estimated entrance length Cencel & Cimbala 2006), hence it was assumed that the flow upon exit was a fully developed turbulent flow. The pipe's angle was measured with a digital inclinometer (GemRed with 0.05° manufacturer-specified accuracy).

The temperature of the water, measured continuously by the flow meter's built-in sensor, ranged from 20.4 °C to 21.8 °C for the smooth hydrophilic and hydrophobic surface experiments ('A' plates in table 1), and from 23.5 °C to 23.9 °C for the rough surface experiments ('B' plates in table 1). Hence the dynamic viscosity and density of the filtered tap water were taken to be $(9.4 \pm 0.4) \times 10^{-4}$ Pa s and 997.5 ± 0.5 kg m^{-3}, respectively. Surface tension was measured utilizing an annular slide (Lapham, Dowling & Schultz 1999) and found to be 72.3 ± 2.3 mN m^{-1} (i.e. within experimental uncertainty of that expected for water, 72 mN m^{-1} at the measured water temperature).

A Labview VI controlled National Instruments USB-6351 DAQ was used to trigger the cameras and measure the transducer outputs. Data were acquired at 30 kHz and then averaged over 0.075 s for each saved data point. Each dataset contained 600 of these averaged data points. 100 data points were taken before the pump was turned on, for zero reference; 400 data points taken during the experiment ensured that the system reached a steady state and yielded ≈28 s of steady data, followed by 100 data points recorded after the pump was turned off to observe the dewetting process and the return of measured quantities to reference values.

2.1. *Contact angle measurement*

The static contact angle of the surfaces was measured by depositing a 2 μl water droplet on top of the surface. As the capillary length for water in normal conditions is 2.74 mm, for the 2 μl droplet of radius ≈0.9 mm, the effect of gravity could be ignored. The droplets were imaged using a Basler ace acA2040-55um camera, and the images (figure 3) analysed in ImageJ, utilizing a contact angle measuring plugin (Daerr & Mogne 2016).

https://doi.org/10.1017/jfm.2022.124 Published online by Cambridge University Press

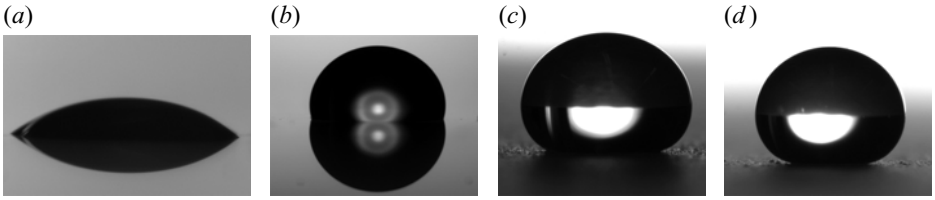

Figure 3. Pictures of droplets taken for the contact angle measurement. Surfaces: (*a*) A1 Glass ($45 \pm 8°$); (*b*) A2 NeverWet ($101 \pm 3°$); (*c*) A4 NaisolSHBC ($142 \pm 4°$); (*d*) A5 Cytonix800M ($150 \pm 2°$).

For each surface, three repeated measurements at five locations in a 254 mm wide cross-pattern were conducted. Table 1 reports the means and standard deviations of these 15 measurements.

2.2. *Roughness measurement*

The roughness of each surface was measured at five different locations, with five readings taken at each location. Additionally, a single measurement at four randomly chosen locations was taken. These 29 measurements per test surface were obtained with a Mitutoyo Surftest SJ-210 roughness meter with resolution 6 nm. Prior to measuring the test surfaces, the device was checked against a roughness calibration plate and yielded a reading within specifications of the calibration plate. The roughness measurements are summarized in table 1, where $\pm$ indicates one standard deviation of the 29 measurements taken per surface. We report the arithmetic average, R_a. This can be related to the non-dimensional roughness, $k^+ = \rho u_\tau k_s/\mu$, where u_τ is the frictional velocity based on measured force and water patch size, and $k_s \approx 5.86R_a$ is the surface sand-grain roughness (Adams, Grant & Watson 2012). As the dimensionless roughness k^+ satisfies $k^+ < 5$ (table 1) for all except the intentionally rough surface B3, surfaces A1, A2, A4, A5 and B1 are considered hydraulically smooth.

2.3. *Test surfaces*

Coatings and plate material were chosen to be transparent to enable the visualization of the water patch through the plate from the top view camera. Four different coatings (listed in table 1) were utilized to examine the effect of hydrophobicity on hydraulically smooth surfaces. Two additional surfaces were prepared for the experiments on the effect of roughness. Both of these were coated with the same primer to try to maintain the same contact angle, but 64.5 ml m^{-2} of ceramic microspheres (Miapoxy 64) with a size distribution from 10 to 540 µm and mean 110 µm were randomly sprinkled onto surface B3. The resulting measured surface properties are summarized in table 1.

Depending on the coating (if it would adhere to glass), two different plate materials were used. For surfaces A1 and A2, 451 mm × 610 mm × 3.2 mm glass plates were employed, while for the rest, 451 mm × 610 mm × 6.4 mm acrylic plates were used. The plate thicknesses were chosen such that, based on theory, deformation due to the plate's mass and the force from the impinging jet would be less than 25 µm.

2.4. *Test matrix*

The range of flow rates (Q), pipe diameters (d), pipe angles (α) and other parameters considered in the present study, as well as fluid properties, are summarized in table 2. The ranges of dimensionless numbers, relevant based on dimensional analysis (discussed

https://doi.org/10.1017/jfm.2022.124 Published online by Cambridge University Press

Parameter	Range	Units
Flow rate (Q) [a]	0.7–13.6	$\mathrm{l\,min^{-1}}$
Pipe diameter (d)	4.7–14	mm
Jet velocity (U) [b]	0.5–5	$\mathrm{m\,s^{-1}}$
Jet angle (α)	15–55	deg.
Surface contact angle (θ)	45–150	deg.
Roughness (R_a)	$11–21 \times 10^3$	nm
Surface tension (σ)	72.3	$\mathrm{mN\,m^{-1}}$
Dynamic viscosity (μ)	$(9.4) \times 10^{-4}$	Pa s
Density (ρ)	998	$\mathrm{kg\,m^{-3}}$
Gravity acceleration (g)	9.81	$\mathrm{m\,s^{-1}}$

Table 2. Parameter ranges explored and water properties at experimental conditions. Note that the jet angle, α, is defined relative to the horizontal plane.
[a]Computed from the measured mass flow rate, $Q = \dot{m}/\rho$.
[b]Average velocity, $U = 4Q/(\pi d^2)$.

Parameter	Range
Weber number $\left(We = \dfrac{\rho d U^2}{\sigma}\right)$	16–4850
Reynolds number $\left(Re = \dfrac{\rho d U}{\mu}\right)$	$2.6–78 \times 10^3$
Bond number $\left(Bo = \dfrac{\rho g d^2}{\sigma}\right)$	3–26.7
Relative roughness $\left(\epsilon = \dfrac{R_a}{d}\right)$	$7.8–44.6 \times 10^{-3}$
Froude number $\left(Fr = \sqrt{\dfrac{We}{Bo}} = \dfrac{U}{\sqrt{gd}}\right)$	1.4–23.2

Table 3. Ranges of the relevant non-dimensional parameters derived in Appendix C. Note that albeit Froude number is not an independent group as it is just a combination of Weber and Bond numbers, its range is listed here for clarity.

further in Appendix C), are given in table 3. We note that the parameter ranges studied were chosen to match, to the extent possible, those expected to be relevant for air layer drag reduction over superhydrophobic surfaces (Callahan-Dudley *et al.* 2020; Peifer *et al.* 2020).

3. Results: effects of hydrophobicity on a smooth surface

We first consider the water spread topology and force on the plate resulting from jet impingement on hydraulically smooth surfaces with different hydrophobicity – the 'A' plates of table 1.

3.1. *Water patch topology*

Figure 4 shows the side and top views for four different flow rates, for the four different 'A' surfaces (A1, A2, A4 and A5 in order of increasing hydrophobicity). The pipe diameter

https://doi.org/10.1017/jfm.2022.124 Published online by Cambridge University Press

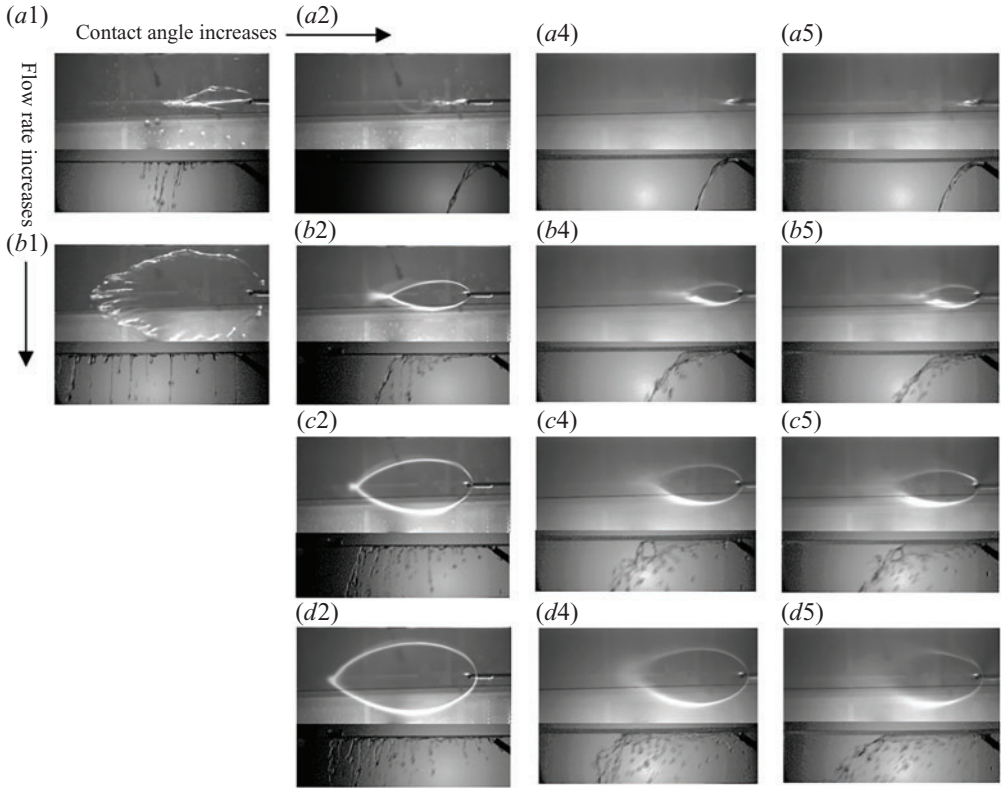

Figure 4. Top view (upper part of each panel) and side view (bottom of each panel) for different jet momentums and surface hydrophobicities. Pipe angle, α, and diameter, d, are constants equal to 35° and 9.3 mm, respectively. Flow rate, Q, from top to bottom row is 2.12, 4.25, 6.4 and 8.52 l min^{-1}. The Reynolds numbers are therefore 5.54×10^3, 1.11×10^4, 1.67×10^4, 2.22×10^4, and the Weber numbers are 45, 181, 411, 728. Surfaces and their contact angles from left to right are: A1 (45°), A2 (101°), A4 (142°) and A5 (150°). The two highest flow rates on the hydrophilic plate, A1, were not reported as the water spread beyond the plate's edges.

(9.3 mm) and angle (35°) are constant in this figure to highlight differences due to only surface wettability and jet momentum. The top view (upper part of each panel) for the hydrophobic surfaces is the average of thousands of images, whereas the side view (bottom of each panel) is an instantaneous still image. Mass flow rates for each row were constant within 4 %, and the only parameter varied within a row was the surface hydrophobicity.

Two different water patch topologies can be distinguished in these data, and can also be found for other pipe angles and flow rates. On hydrophobic surfaces, the impinging jet spreads in an ellipse-like nearly 'falling droplet' shape (figure 6*a*). Two rims enclose a thin film of liquid flowing between them, which is presumed to be laminar as the Reynolds number, based on downstream distance, would be below transitional, and the film surface is free of observable perturbation. The rims are pushed outwards due to the inertia of the impacting jet, increasing the wetted region's width $b(x)$ until approximately half of the patch length, $L/2$ (see figure 5). At this point of maximum width, b_{max}, all the perpendicular-to-the-plate (z) jet kinetic energy is transformed into surface energy (with some losses due to viscosity). During the second half of the patch, the surface energy is

https://doi.org/10.1017/jfm.2022.124 Published online by Cambridge University Press

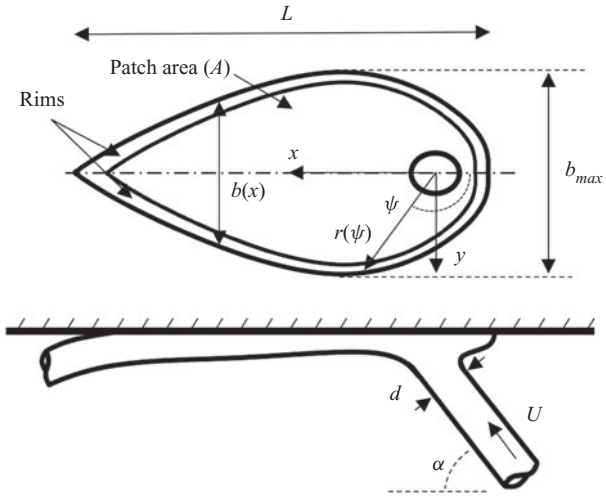

Figure 5. Schematic top view of topology. Main variables are: $b(x)$, water patch width; L, water patch length; A, water patch (wet) area; ψ, angle from the symmetry line; $r(\psi)$, radial coordinate of the water patch edge. Note that all lengths and areas include rims.

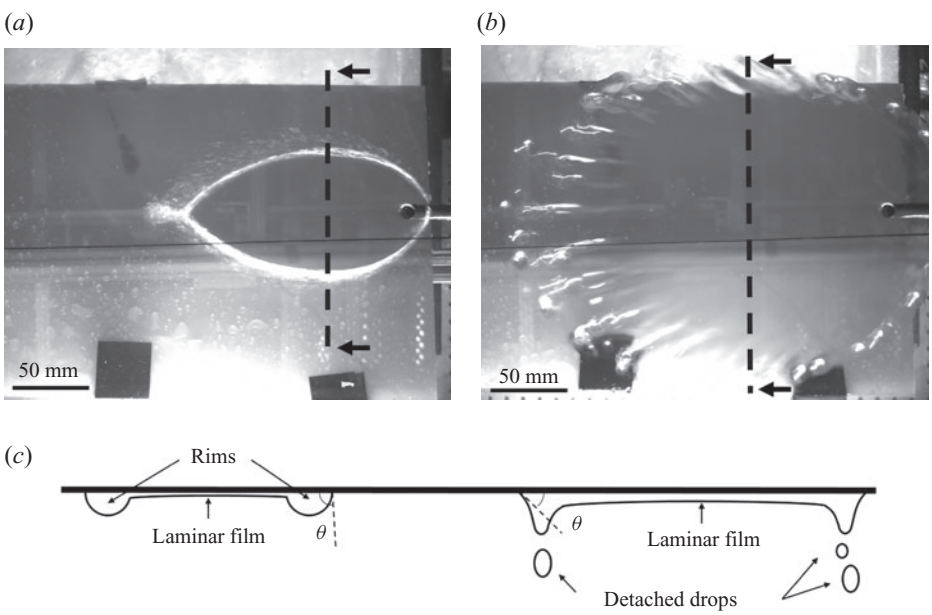

Figure 6. Jet impingement with $Q = 4.8\,\mathrm{l\,min^{-1}}$, $d = 9.3\,\mathrm{mm}$ and $\alpha = 45^\circ$ ($Re = 1.25 \times 10^4$, $We = 231$). (*a*) Top view of patch on a hydrophobic surface (A2). Note the two thick perturbed (hence opaque) rims around a thin laminar (clear) region in the middle. (*b*) Top view of the patch on a hydrophilic surface (A1). The rims are absent, and water accumulates at the edges of the wetted spot from where drops detach (with radial accumulation location being time dependent). Note also the much larger wetted area on the hydrophilic surface. (*c*) Sketches of the approximated cross-section views at the lines indicated in (*a*,*b*); $\theta \approx \theta_{static}$ is the contact angle at the edge of the water patch.

transformed back into kinetic energy, pulling the rims together until they merge and detach from the plate.

On hydrophilic surfaces (figure 6*b*), we find a significantly different topology. No rims are observed and the water spreads based on initial kinetic energy in all directions, as

https://doi.org/10.1017/jfm.2022.124 Published online by Cambridge University Press

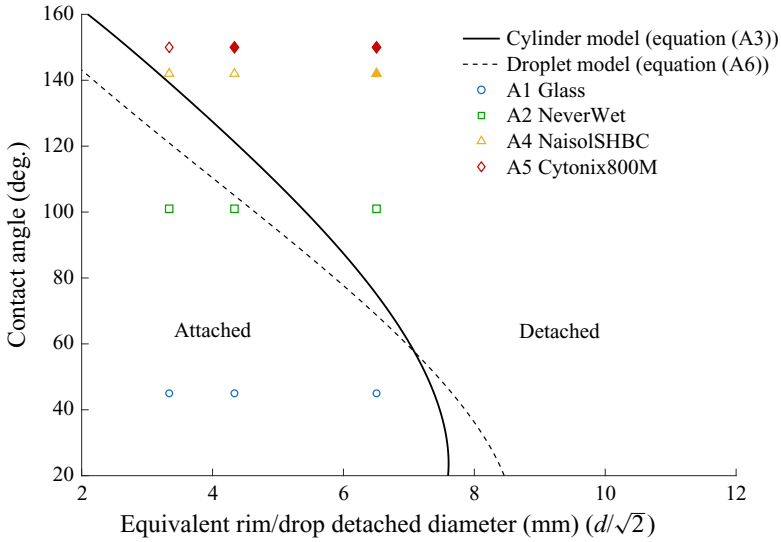

Figure 7. Map of the experimental conditions and the critical rim diameter (see (A3)) above which the rim is expected to not be able to remain attached. Symbols indicate experimental observations: empty symbols indicate cases where the rims remained attached until they merged or water was stopped by viscosity and pooled on the edges; filled markers indicate that detachment was observed before rims merged. The dashed line (see (A6)) shows the critical diameter for droplets.

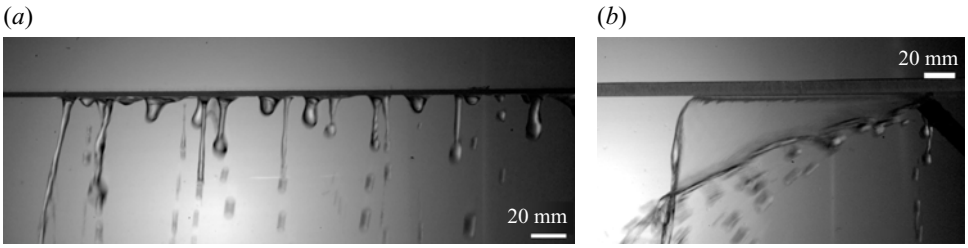

Figure 8. (*a*) Detachment from a hydrophilic surface (A1); $Q = 2.46\,\mathrm{l\,min^{-1}}$, $d = 6.1\,\mathrm{mm}$ and $\alpha = 35^\circ$ ($Re = 9.75 \times 10^3$, $We = 212$). (*b*) Continuous rim/edge and film detachment on the superhydrophobic surface (A5); $Q = 4.62\,\mathrm{l\,min^{-1}}$, $d = 9.3\,\mathrm{mm}$ and $\alpha = 45^\circ$ ($Re = 1.21 \times 10^4$, $We = 214$).

discussed in Kate *et al.* (2007), in the context of impingement on a top surface. For the range of parameters examined, water does not detach from the plate until it accumulates on the edges, once its advance is halted by frictional drag (Bhagat *et al.* 2018). Once enough water accumulates, gravity overcomes surface tension and a drop falls. The drops fall nominally vertically, which indicates that all momentum parallel to the plate was lost (see figure 8*a*). Droplets with a certain radius fall periodically from the edges, as was described previously for jet impacts on the underside of a hydrophilic flat plate by Jameson *et al.* (2010) and Brunet, Clanet & Limat (2004). An energy argument, similar to that described in (A1), but for spherical drops ((A6) and dashed line in figure 7), predicts the size of falling droplets to be around 8 mm, which is in fair agreement with observation in the present work (e.g. figure 8(*a*) shows falling droplets with diameters around 10 mm). Randomness in the location from which droplets detach may be caused by a Rayleigh–Plateau type instability, but further analysis would be needed to verify this.

https://doi.org/10.1017/jfm.2022.124 Published online by Cambridge University Press

3.1.1. *Simplified criteria for water detachment*

Seeking to better understand the different detachment behaviours observed on hydrophilic and hydrophobic surfaces, we derive in Appendix A a simplified model for a critical detachment rim radius of the water as a function of the surface contact angle. On hydrophobic surfaces, we could expect rims to detach from the underside of the plate if they had radius larger than that indicated in (A3). The critical rim diameter, $2r_D(\theta)$, is plotted as a continuous line in figure 7. To the left of the line, the energy of the attached rim is lower than that of the detached rim, therefore we expect that it will preferably stay attached. To the right of the line, on the contrary, detachment is energetically favourable. In figure 7, each point represents the approximate rim diameter for all the pipe angles α and flow rate Q for each surface and pipe size. Such a rim diameter was computed, as a first approximation, neglecting the flow rate through the thin laminar film between the rims. Detached (filled symbol) status was given to those flows where rims detached even before they merge (e.g. as seen in figure 8*b*), and attached (empty symbol) status indicates cases where rims detached only after merging (e.g. panel (*d*4) of figure 4), or a hydrophilic surface where the water accumulated at the edge of the patch and fell as droplets (figure 6*b*).

Equation (A3) predicted that on the mildly hydrophobic surface (A2), all but the largest jets are small enough to allow the water to remain attached, even if rims form. However, we see that rim separation (filled symbols in figure 7) required an ≈20 % larger equivalent rim diameter to detach than was predicted. Interestingly, if we do not neglect the flow rate in film between the rims and assume this to be ≈30 % of Q, then the data points would be shifted to the left, matching the model's prediction.

Figure 7 shows superhydrophobic surfaces (A4 NaisolSHBC and A5 Cytonix800M) on the detached region of the graph, to the right of the borderline. In this case, where detachment is favoured from an energy balance viewpoint, we observe experimentally the rims or even the full film detach from the surface before the rims merge. For example, in figures 4(*d*4,*d*5) we see the rims detach, and in figure 8(*b*) even the full film detaches. For hydrophilic surfaces, where detachment is not energetically favourable, water detached in drops once forward momentum was lost and water accumulated in the path edges, as indicated by the droplets falling nearly straight down (figure 8*a*). (Similar droplet separations from surface considerations are provided e.g. in the numerical study of Manik, Dalal & Natarajan 2019).

3.2. *Water patch width*

Another key result of water spreading on surfaces is the maximum width. From conservation of mass, momentum and energy, we can attempt to predict the maximum width of the water patch as a function of the jet's vertical momentum, surface tension and contact angle. Appendix B discusses such a simplified model in detail. For a surface in Wenzel state, ignoring viscosity, we find that the water patch width is expected to scale with the contact-angle-modified Weber number of the perpendicular jet velocity component, $We_{\theta z} = \rho d u_z^2/\sigma(1-\cos\theta)$ as

$$\frac{b_{max}}{d} = \frac{\pi}{8\cos\alpha} We_{\theta z} + \frac{\pi}{\cos\alpha(1-\cos\theta)}. \tag{3.1}$$

The maximum water patch width is plotted in figure 9 against $We_{\theta z}$. The model in (3.1) for smallest and highest α is represented by two lines.

https://doi.org/10.1017/jfm.2022.124 Published online by Cambridge University Press

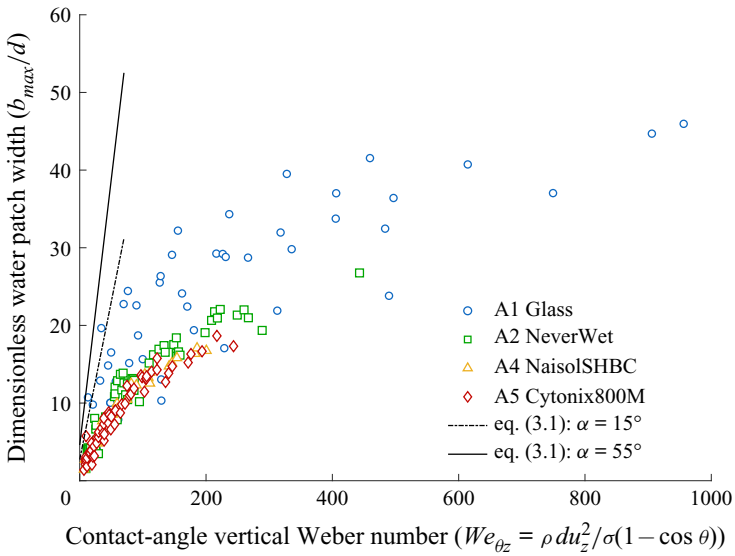

Figure 9. Jet-width-normalized maximum water patch width versus contact-angle-modified vertical-velocity Weber number $We_{\theta z}$. Lines show predictions of (3.1) for lowest and highest jet angle α.

Data seem to collapse when plotted against the mentioned contact-angle Weber number (see figure 9), and furthermore, at low Weber numbers, the data also show a linear trend, albeit at a lesser slope than expected based on the simple analysis. However, the linear trend is lost as the jet speed increases, and viscous frictional losses could be expected to become non-negligible in the larger water patch. While (3.1) guided us to collapse the data with $We_{\theta z}$, it is overly simplified especially in respect of ignoring friction.

A more comprehensive model was proposed by Wang *et al.* (2013). Starting from the results of Wilson *et al.* (2012), Wang *et al.* (2013) construct a model for jet impingements on a vertical surface, accounting for oblique jet impact by incorporating the radial flow distribution model developed by Kate *et al.* (2007). While Wang *et al.* (2013) are mainly concerned with jet impingement on a vertical surface, they also presented a model ignoring the effect of gravity, and such a model could be expected to more closely match the present data. The simplified version of this model yields the extent of the radial flow zone (corresponding to our patch width minus rim thickness) as a function of angular coordinate ψ and the impinging jet radius r_0:

$$r(\psi) = \left(\frac{9}{50} U^3 \frac{\sin^9 \alpha}{(1+\cos\alpha\cos\psi)^6} \frac{r_o^6 \rho^2}{\mu\sigma(1-\cos\theta)} \right)^{1/4}. \tag{3.2}$$

From this result, it is possible to obtain analytically the maximum width of the radial flow zone. Noting the width $b = 2r(\psi)\sin\psi$, we can obtain the maximum width by finding the maximum of the term $\sin^2\psi/(1-\cos\alpha\cos\psi)^3$ (Wang *et al.* 2013). Reorganizing terms, using $d = 2r_0$, and recognizing the modified Weber number ($We_{\theta z}$) and Reynolds number (Re), it is possible to express the maximum patch width as

$$\frac{b_{max}}{d} = 0.4606 \left(\frac{\sin^7\alpha \sin^4\psi^*}{(1+\cos\alpha\cos\psi^*)^6} We_{\theta z} Re \right)^{1/4}, \tag{3.3}$$

https://doi.org/10.1017/jfm.2022.124 Published online by Cambridge University Press

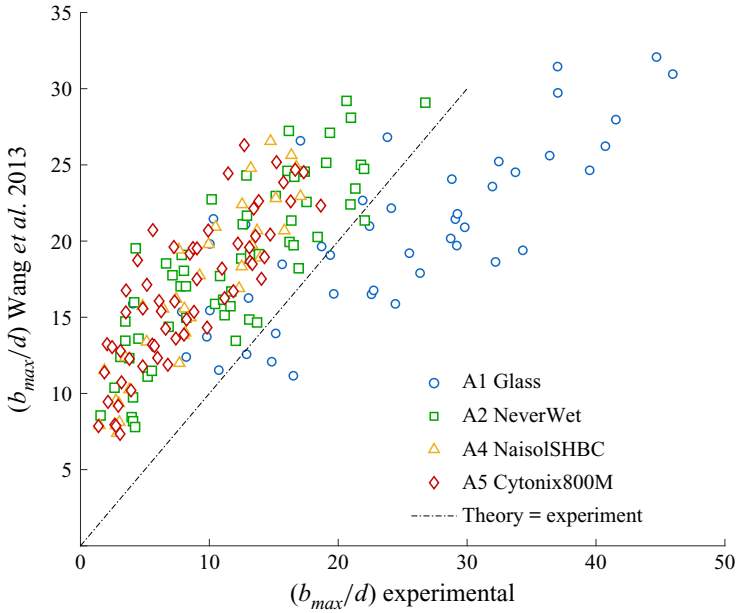

Figure 10. Comparison of measured patch width to width of radial spreading zone predicted by (3.3) based on model by Wang *et al.* (2013).

where ψ^* corresponds to the azimuthal angle for maximum width obtained through the minimization of the $\sin^2\psi/(1-\cos\alpha\cos^3\psi)$ term, such that

$$\cos\psi^* = \frac{1-\sqrt{1+3\cos^2\alpha}}{\cos\alpha}. \tag{3.4}$$

The comparison of the predicted radial flow zone width to our data is presented in figure 10 and shows fair agreement with the experimental data. Although the trend is well captured, the tendency of the Wang *et al.* (2013) model is to overestimate the radial flow zone width, even though our definition of the width also includes the rims. However, this overestimation of the patch width is not surprising as nothing in the models accounts for the tendency of gravity, particularly on superhydrophobic surfaces, to promote early dewetting. An extreme case of this is seen in figure 8(*b*), which shows a 'skewed water bell' where the film clearly separates from the plate before the radial spread was expected to end. A potential additional difference is that – contrary to the Wang *et al.* (2013) assumption that all momentum of the flow along a streamline at all angles ψ is balanced by the surface tension at the edges of the radial flow zone – at maximum width (which does not occur at $\psi = 90^\circ$), the flow in the rims still carries momentum in the streamwise direction, and the boundary condition could be amended accordingly.

3.3. *Water patch length*

The normalized water patch length is another quantity of interest. As seen in figure 11, it appears to scale approximately with the square root of the contact-angle-modified Weber number based on the horizontal, x, jet velocity component:

$$We_{\theta x} = \frac{\rho d u_x^2}{\sigma(1-\cos\theta)}. \tag{3.5}$$

https://doi.org/10.1017/jfm.2022.124 Published online by Cambridge University Press

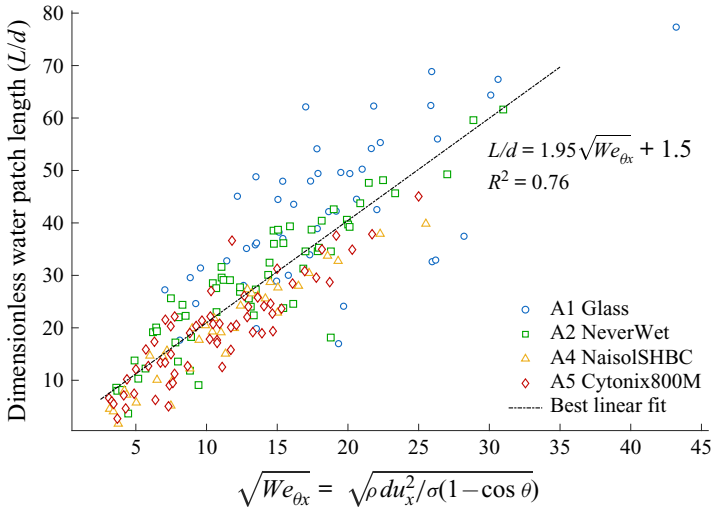

Figure 11. Jet-width-diameter normalized water patch length plotted against the square root of the contact-angle-modified horizontal-velocity Weber number, $We_{\theta x}$.

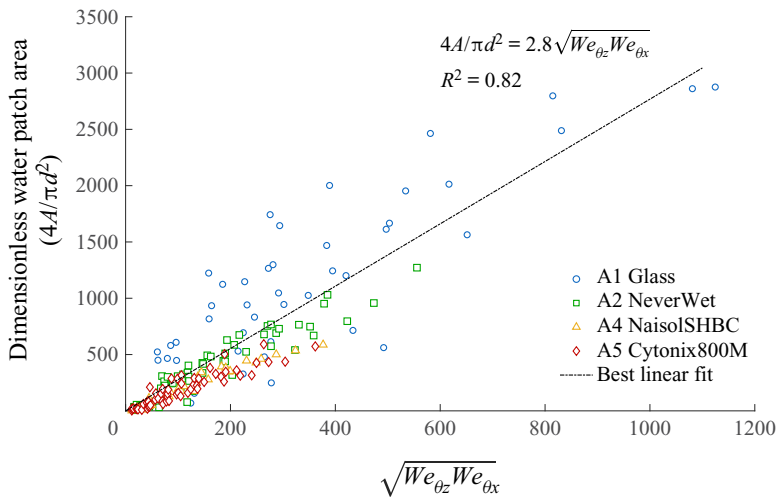

Figure 12. Normalized water patch area plotted against the square root of the product of contact-angle-modified Weber numbers ($We_{\theta i} = \rho u_i^2 d/\sigma(1-\cos\theta)$).

We also note that a similar modified Weber number has been employed by e.g. Son & Kim (2009) to characterize the spreading diameter of an inkjet droplet.

3.4. *Water patch area*

Given the trends of water patch width and length (the former scaling with the normal, z, and the latter with the square root of the x-component with the contact-angle-modified Weber number), the water patch area was expected to potentially scale linearly with the square root of the product of the two contact-angle-modified Weber numbers. This assumption appears to be a fair approximation, as shown in figure 12.

https://doi.org/10.1017/jfm.2022.124 Published online by Cambridge University Press

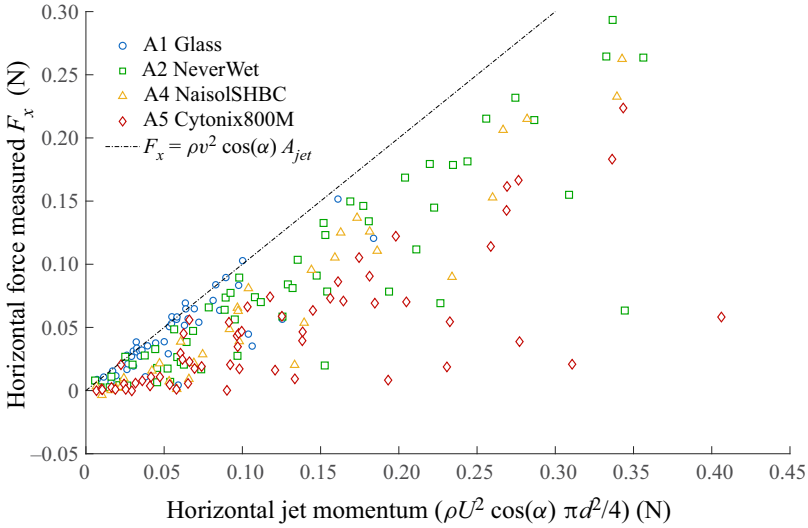

Figure 13. Measured horizontal force on the plate versus horizontal momentum of the incoming jet; the dashed line represents (3.6), where these are equal and all horizontal momentum is lost due to viscous friction. Data below the line represent cases where only a fraction of the momentum was lost.

3.5. *Force on plate*

Finally, the force on the plate was measured. Considering a control volume around the plate and encompassing the jet and water patch, the jet's momentum loss in the horizontal direction is equal to the measured force on the plate, if we assume air–water drag to be negligible:

$$F_x = \dot{m} u_x = \left(\rho U d^2 \frac{\pi}{4}\right)(U \cos\alpha), \tag{3.6}$$

where α is the incident jet angle, nominally taken as the pipe angle, and $\dot{m}$ is the jet's mass flow rate.

In figure 13 the force measured by the load cell is plotted against the incoming jet's horizontal momentum, and (3.6) is plotted as a dashed line. Points on the dashed line hence correspond to cases where all of the jet's horizontal momentum is lost, and points below this line are cases where water departs the plate before losing all the momentum. We observe that most of the data for impingement of a hydrophilic surface (A1) lie on the line, thus indicating that all incoming horizontal momentum was lost due frictional drag. This is in good agreement with observations of water departing the glass as droplets with nominally no horizontal velocity, as seen in figure 14(*b*). Jet impingement on (super)hydrophobic surfaces populates below the line in figure 13, which indicates that water detaches from the low-energy surface before losing all its momentum. We see this in figure 14(*a*), where water departs the hydrophobic surface at nearly the same angle as it impacted.

From these data, we find the force on the plate to be dependent on the jet angle, jet velocity, surface properties and jet diameter. As we also have a measurement of the water patch area, A, we can evaluate the frictional drag coefficient, $C_F = F_x/\frac{1}{2}\rho u_x^2 A$. Figure 15 plots C_F based on measured force and patch area against the Reynolds number $Re_L = \rho u_x L/\mu$ based on measured water patch length L and horizontal velocity u_x. In this figure, we also show what C_F would have been on a smooth surface simply assuming

https://doi.org/10.1017/jfm.2022.124 Published online by Cambridge University Press

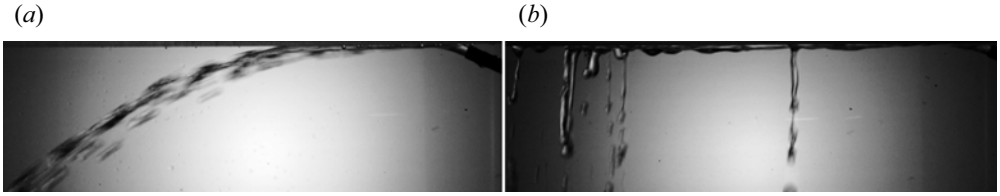

Figure 14. (*a*) 'Rebound' off the superhydrophobic plate (A5); $Q = 2.58\,\mathrm{l\,min^{-1}}$, $d = 6.1$ mm and $\alpha = 25\,^{\circ}$. (*b*) Water departing vertically from a hydrophilic plate (A1); $Q = 1.98\,\mathrm{l\,min^{-1}}$, $d = 6.3$ mm and $\alpha = 25\,^{\circ}$. The jet is at an oblique angle from the right.

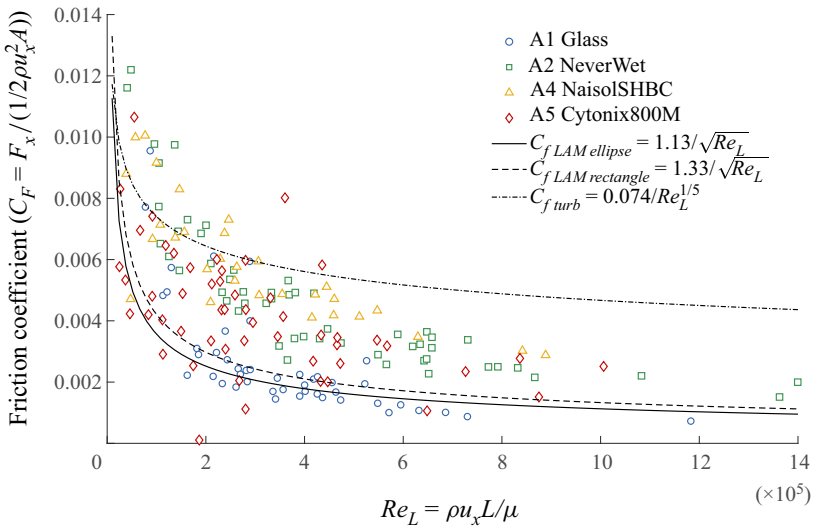

Figure 15. Frictional drag coefficient C_F based on measured horizontal force F_x and patch area A, versus Re_L. The dashed and dash-dot lines represent drag from turbulent and laminar approximations to the boundary layer friction coefficient, if we simplify the patch to be rectangular spanwise uniform. The solid line accounts for elliptical shape for a laminar boundary layer.

a 'rectangular' uniform patch with a Blasius laminar (dashed line) or Prandtl turbulent boundary layer (dash-dot line). For laminar flow, we also considered the nominally elliptical shape in the integration:

$$C_{f,LAMellipse} = \frac{4}{\pi b L}\int_0^L \int_{-b\sqrt{x/L(1-x/L)}}^{b\sqrt{x/L(1-x/L)}} \frac{0.664}{\sqrt{Re_x}}\,\mathrm{d}y\,\mathrm{d}x = \frac{1.13}{\sqrt{Re_L}}. \tag{3.7}$$

This result is shown in figure 15 as the solid line, which best matches the data on a hydrophilic (glass) surface.

While the net force measured was smaller for superhydrophobic surfaces, a higher C_F was estimated based on patch area at given Re_L (see figure 15). This suggests that in the present case, the force reduction is primarily a result of the reduction in the wetted area, and not due to drag reduction over the wetted area. That is, there is no clear sign of viscous shear stress reduction on the wetted patch due to the surface that may trap gas (as discussed in e.g. Gose *et al.* 2018). This may be due to roughness, or a lack of significant amounts of gas trapped on the surface perhaps due to the non-negligible jet impact velocity, similar to the case discussed in Zheng, Yu & Zhao (2005).

https://doi.org/10.1017/jfm.2022.124 Published online by Cambridge University Press

Study	Surface	Contact angle (deg.)
Present study	Underside, horizontal	45–150
Kate *et al.* (2007)	Top, horizontal	Glass ≈45
Wang *et al.* (2013)	Vertical	40–72.5
Kibar & Yiğit (2018)	Vertical	93–117
Kibar *et al.* (2010)	Vertical	102–167

Table 4. Range of surface parameters of the present and previous studies.

Study	Q (l min^{-1})	d (mm)	Re	We
Present study	0.7–13.6	4.7–150	$(2.6–78) \times 10^3$	16–4850
Kate *et al.* (2007)	Not reported	4–10	$(4–10) \times 10^3$	Not reported
Wang *et al.* (2013)	0.43–8	2–4	$(2.2–20.3) \times 10^3$	Not reported
Kibar & Yiğit (2018)	0.13–0.43	1.75	$(1.8–6) \times 10^3$	20–300
Kibar *et al.* (2010)	0.072–3.77	1.75; 4	$(0.5–8) \times 10^3$	5–650

Table 5. Range of flow parameters of the present and previous studies.

4. Results: effect of gravity

Previous studies on jets impacting vertical walls and top sides of surfaces provide interesting data for comparison in order to understand the effect of gravity. Results from four previous studies are used for comparison with current results: Kate *et al.* (2007) had a water jet impact the top of a surface and studied the hydraulic jump that resulted; Kibar *et al.* (2010) and Kibar & Yiğit (2018) performed experimental work on water jet impingement on a vertical (super)hydrophobic surface; and Wang *et al.* (2013) utilized experiment and theory to consider jet impingement on vertical hydrophilic surfaces. The parameter ranges that these investigators examined are compared to ours in tables 4 and 5. We proceed to a quantitative comparison of our data and the results from these previous studies. (And a more extensive qualitative comparison of different water patch topologies observed in the present work and in several other previous studies is provided in figure 18.)

4.1. *Gravity's effect on the wetted area*

Both Kate *et al.* (2007) and Wang *et al.* (2013) theoretically, and later Kibar (2018) by fitting experimental data, developed models to compute the radius of the water patch or hydraulic jump border depending on the azimuthal coordinate ($r = r(\psi)$, see figure 5). Kate *et al.* (2007) obtained the radial location of the hydraulic jump by applying the continuity and momentum equations to a radial slice of the flow. Assuming a quadratic velocity profile in the film, the following relation for the location of the hydraulic jump was obtained:

$$r(\alpha, \psi) = C \left(\frac{d^2}{8} \frac{\sin \alpha^3}{(1 + \cos \alpha \cos \psi)^2} U \right)^{5/8} \nu^{-3/8} g^{-1/8}, \tag{4.1}$$

where C is a constant, ν is the water kinematic viscosity, ψ is the azimuthal coordinate (see figure 5), α is the angle of the jet with the horizontal, and g is the gravitational acceleration. (Note that the effect of the contact angle was not considered in (4.1).)

https://doi.org/10.1017/jfm.2022.124 Published online by Cambridge University Press

For jet impingement on a vertical hydrophilic surface, as discussed in § 3.2, Wang *et al.* (2013) developed a model building on the results of Kate *et al.* (2007) and Wilson *et al.* (2012), obtaining the water patch edge as the position at which the radial flow momentum is equal to the surface tension:

$$R(\psi) = \frac{3U\rho r_e^2 \sin\alpha}{5\sigma(1-\cos\theta)} U_R(\psi), \tag{4.2}$$

where $U_R(\psi)$ is the speed at the water patch edge $r = R(\psi)$, and r_e is the radial position of the impinging jet (Kate *et al.* 2007). The speed in the radial flow film can be obtained from a momentum balance as (Wang *et al.* 2013)

$$\frac{\mathrm{d}u}{\mathrm{d}r} = -10\,\frac{\nu}{U^2 r_e^4 \sin\alpha^2}\, r^2 u^2 - \frac{5g}{6}\,\frac{\cos\psi}{u}. \tag{4.3}$$

Neglecting gravity and assuming large water patches in comparison with the jet diameter ($R \gg d$ and $U_R \ll U$), the above equation can be simplified to obtain (3.2). Since no gravity is included, (3.2) is of interest for impingement on horizontal surfaces.

Finally, Kibar (2018), based on the experimental work in Kibar *et al.* (2010), found an empirical fit for the water patch that resulted from jet impingement on vertical (super)hydrophobic surfaces. The empirical fit that they found for the radial location of the water patch edge was

$$r(\psi) = \frac{d}{2} 0.2\, Re^{0.3}\, We^{0.4} [1+\cos(\pi-\theta)]^{-0.5} \times \left[\frac{\sin^{2.2}\alpha}{1+\cos\alpha\cos\psi}\right]^{1.34} \left[e^{\psi/\pi}\right]^{0.65} \tag{4.4}$$

These theoretical and empirical equations (4.1), (4.2), (3.2) and (4.4), which the previous investigators found to match their data in a satisfactory manner, enable comparison of water patch topology depending on the plate's orientation i.e. effect of gravity (for a limited range of parameters, as the parameter ranges considered in present study only partially overlapped those previously considered, see tables 4 and 5).

A comparison of the water patch shape for a particular set of parameters is depicted in figure 16. All the shapes are similar, but enlarged by a factor that varies depending on the flow conditions, primarily differing in orientation of gravity. For most cases, the patch on the underside of the plate had an area between 1 and 5 times smaller than on vertical surfaces and the top side. This is not surprising given that in our case, water can detach once gravity overcomes surface tension.

Figure 17 shows the average ratio of water patch length based on (4.1), (4.2), (3.2) and (4.4) with respect to that seen in the present study. Comparison with Kate *et al.* (2007) is particularly interesting. We observe that for a hydrophilic surface (in our case A1 Glass), the length ratio is approximately 1, which suggests that for the parameter range being considered and in the case of a hydrophilic surface, the dominant mechanisms are the same regardless of the orientation of gravity. That is, inertia and viscosity dominate the water patch size. On the top of a surface, a hydraulic jump results where momentum is mostly lost and jump conditions are met, whereas on the underside of a plate, the hydraulic jump is substituted by water accumulation at the corresponding location until gravity leads to droplet detachment, as discussed in § 3.1.1. However, when the surface impacted is hydrophobic, while still within parameter range of Kate *et al.* (2007), area ratio begins to increase. Surface tension still has the role of containing the water spread, but on the underside of a plate, gravity facilitates dewetting when the two rims merge

https://doi.org/10.1017/jfm.2022.124 Published online by Cambridge University Press

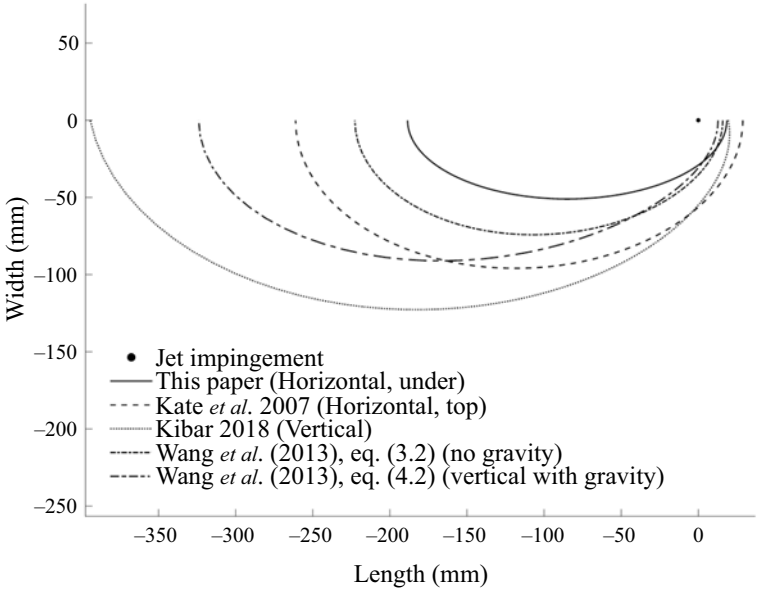

Figure 16. Water patch shape comparison between current paper and equations found to fit results of: Kibar (2018), see (4.4); Wang *et al.* (2013), see (3.2) and (4.2); and Kate *et al.* (2007), see (4.1). Here, $Q = 4.8\,\mathrm{l\,min^{-1}}$, $d = 9.3\,\mathrm{mm}$, $\theta = 101^\circ$ and $\alpha = 45^\circ$ ($Re = 1.25 \times 10^4$, $We = 231$).

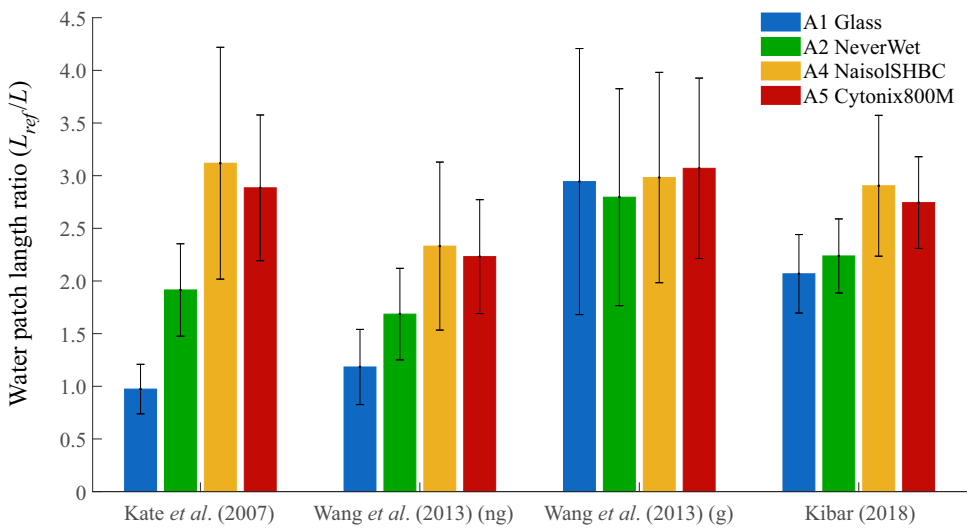

Figure 17. Mean length ratio for Kibar (2018), Wang *et al.* (2013) (*g* for gravity included, (4.2), and *ng* for no gravity, (3.2)) and Kate *et al.* (2007) with respect to this paper. Each bar value is the average of the ratio of all the tests done of such surface (51 for A1 Glass, 68 for A2 NeverWet, 35 for A4 NaisolSHBC, and 64 for A5 Cytonix800M). The error bars represent one standard deviation.

(e.g. panels (*b*1) and (*b*2) of figure 4), or even before (e.g. figure 8*b*). The key difference is that with the present orientation of gravity, the impingement does not need to result in a hydraulic jump, but rather fluid can dewet the surface prior to a hydraulic jump.

https://doi.org/10.1017/jfm.2022.124 Published online by Cambridge University Press

Comparison to a water patch on a vertically orientated surface of Wang *et al.* (2013) (with gravity, (4.2)) and Kibar (2018) shows that the water patch length is 2–5 times that found in the present study. However, when gravity is omitted from the model, Wang *et al.* (2013) is closer to this paper's results. Note also that the width that Wang *et al.* (2013) predict is that of the radial flow zone alone, and our definition of the water patch width includes this zone and the rims. Hence a ratio slightly below unity would indicate that the model prediction matches the present data. In these previous studies, surface tension had a role along with viscosity and inertia, and gravity aided the spread of the fluid but did not promote dewetting. This differs from the case in the present study, where gravity aids the dewetting from the underside of the surface, resulting in smaller water patch areas.

Furthermore, to check if changing the orientation of gravity would have a similar effect on topology resulting from jet impingement on our specific surfaces, a quick and rough qualitative experiment was conducted by affixing a pipe at an angle to one of our plates (A4). When manually varying the angle of the entire set-up, an increase in wetted patch area was observed, and this was qualitatively in agreement with Wang *et al.* (2013); Kibar (2018). Hence for this type of experiment and parameter range, a relatively low Froude number and orientation of gravity appear to have a major role in determining the water patch area.

4.2. *Gravity's effect on force imparted on plate*

In Kibar *et al.* (2010), which spanned $Re = 500$–8000, $We = 5$–650, $\alpha = 15$–45°, and examined surfaces with $\theta = 102^\circ, 112^\circ, 123^\circ, 145^\circ, 167^\circ$, the force ratio with respect to the momentum of jet imparted on the plate was found to have fair agreement with an empirical fit given by

$$\frac{F_x}{M_{jet,x}} = 0.911\, Re^{0.481}\, We^{-0.524}(1+\cos(180-\theta))^{-7.188}\sin(\alpha)^{0.529}\left(\frac{4A}{\pi d^2}\right)^{0.690}, \quad (4.5)$$

where $M_{jet,x} = \rho Q U \cos(\alpha)$. When (4.5) is applied to our full range of parameters, non-physical results exist that exceed the force–momentum ratio of unity. However, if only cases within the range of data of (Kibar *et al.* 2010) are considered, then the effect of gravity being parallel to the plate (where the plate is in a vertical position as in Kibar *et al.* 2010) significantly increases the force on the plate (around an order of magnitude for a glass surface, by a factor of 3–5 times in the case of (super)hydrophobic surfaces). This is presumably due to the significantly increased contact area and allowing for increased effect from frictional drag.

However, as only a small number of cases in the present study overlap with Reynolds and Weber numbers considered in Kibar *et al.* (2010), whose empirical correlation cannot be extrapolated beyond the original parameter range, further study would be needed to quantify the effect of orientation on jet momentum loss (i.e. force on the plate).

4.3. *Gravity's effect on the topology*

While qualitatively similar topology to figures 4 and 6 was found for jet impingement on vertical and horizontal (super)hydrophobic surfaces in Kibar (2018), Kibar *et al.* (2010) and Kaps *et al.* (2014), in general, multiple topologies can be identified for jet impingement on surfaces depending on the orientation of gravity. Figure 18 shows the various topologies

https://doi.org/10.1017/jfm.2022.124 Published online by Cambridge University Press

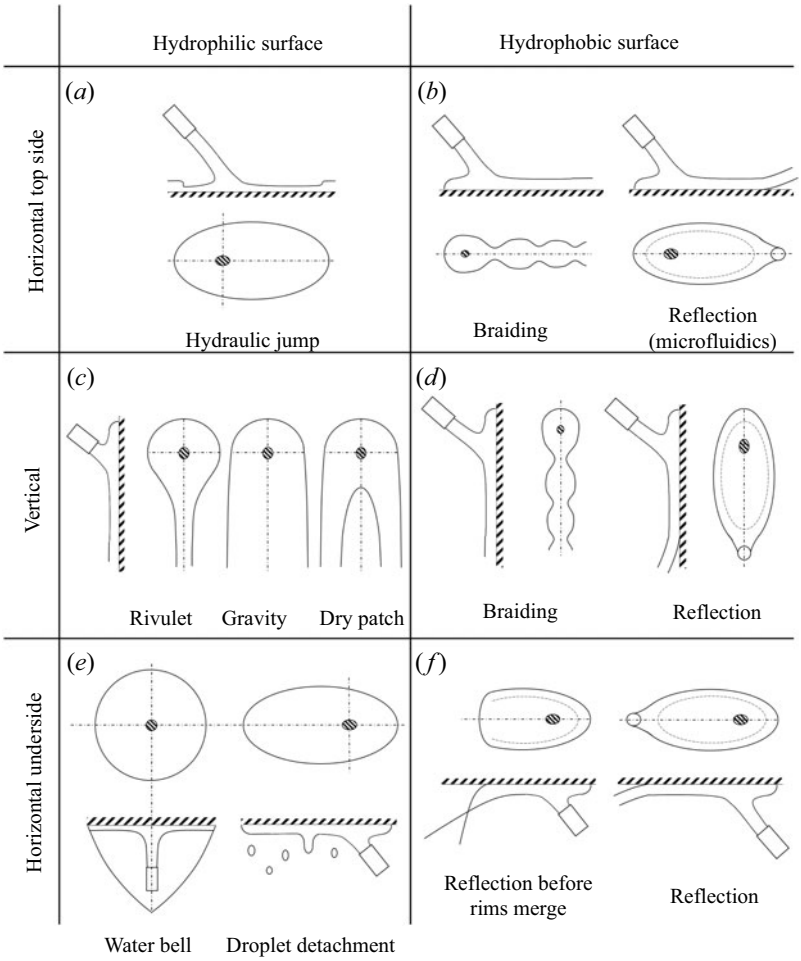

Figure 18. Different water patch topologies and flow patterns reported depending on plate orientation and contact angle. (*a*) Hydraulic jumps as seen in Kate *et al.* (2007). (*b*) Braiding as seen in Mertens, Putkaradze & Vorobieff (2005), and reflections for microjets as in Celestini *et al.* (2010). (*c*) Vertical rivulet flow (Wilson *et al.* 2012), gravity and dry patch flow (Wang *et al.* 2013). (*d*) Braiding and reflection of jet as per Kibar *et al.* (2010). (*e*) Underside waterbells for limited range of flow conditions of Button *et al.* (2010), and droplet detachment as seen both in Button *et al.* (2010) and in the present study on surface A1. (*f*) Reflection before rims join, forming a skewed water bell, and reflection when rims merge, as seen in the present study on surfaces A2, A4 and A5.

reported for different orientations of gravity and contact angle, as well as those seen in the present study (panel (*e*) right, and (*f*) left and right).

With respect to a jet impinging on the top side of a hydrophilic horizontal plate, several topologies of hydraulic jumps are explained and modelled in (Kate *et al.* 2007). Braiding appears when the surface starts to transition towards the hydrophobic region (Celestini *et al.* 2010) or when the plate has some inclination with respect to gravity (Mertens *et al.* 2005). Finally, reflections were seen when very high surface hydrophobicity and small jets were used (Celestini *et al.* 2010).

If the plate is vertical, then rims form on the edges of the water patch, resulting in rivulet flow at low flow rates (Wilson *et al.* 2012), and when the jet flow rate increased, 'gravity' or

https://doi.org/10.1017/jfm.2022.124 Published online by Cambridge University Press

'dry patch' patterns (figure 18*c*) have been reported (Wang *et al.* 2013). Higher angles of jet impingement, α, or jet momentum tend to lead to what authors called 'gravity' flow, while increasing the contact angle (albeit within the hydrophilic region) increased the tendency for rivulet and dry patches. That is, as in the present study, increased hydrophobicity reduced the surface-water contact area. If the vertical walls' contact angle is increased above 90° into the hydrophobic and superhydrophobic ranges, then braiding was reported for lower contact angles and jet flow rate, while higher values of these parameters led to transition towards reflection, and even splashing (i.e. disorganized reflection).

Finally, if the jet impinges on the underside of a horizontal hydrophilic surface, as in the present study (figure 8*a*), the result was droplet detachment from the edges. Interestingly, for a laminar jet impinging normal to a surface, and for a special combination of parameters, a water bell topology may also result as in Button *et al.* (2010). In the present study, if surface hydrophobicity is increased, then reflection can be observed (similar to that seen in the case of vertical surfaces), although the water patch area is greatly reduced. And a skewed-water-bell-type detachment (figure 8*b*) could be observed in some particular cases.

Comparing to previous hydrophobic surface experiments where the orientation of gravity was different, the jet impinging on the plate's underside differs notably: e.g. the rims do not reappear after merging, and a second patch never forms for the parameter range studied. For all conditions examined, once the rims merge, water detaches from the plate in a jet-like topology. This is substantially different from observations of Kibar *et al.* (2010), who studied a jet with parameter range overlapping ours and reported oscillation between open and closed rims, i.e. 'braiding'. This braiding could be considered to be the two-dimensional (due to the physical surface) equivalent to fluid chains studied in context of two liquid jets impinging in air (e.g. Bush & Hasha 2004), and qualitative similarity to flows of the present study can be noted in the rim and film topology. However, differences arise due to the effect of gravity, because of the present study's lower Froude numbers and the presence of a solid surface.

5. Results: effect of roughness

We also conducted exploratory experiments on the effect of surface roughness on the flow topology. Surfaces B1 (smooth) and B2 (rough), described in table 1, have similar contact angles, but B2 is hydraulically rough. For water patch area, shown in figure 19, we can see a trend: for low jet momentum, the wetted area on surfaces is similar. However, beyond a 'critical' $\sqrt{We_{\theta z} We_{\theta x}} \approx 60$, the smooth surface's wetted area is more than double the size of that on the rough surfaces.

Considering the low Weber number region where the viscous sublayer would be thicker, it could be that effectively both surfaces present to the flow as hydraulically smooth in this range. As the viscous sublayer becomes thinner at higher velocities (higher *We*), the surface of the B2 plate becomes hydraulically rough, and lower water patch areas occur due to higher momentum loss as a result of increased skin friction.

Jet impingements at three different flow rates are shown in figure 20. The images in figure 20(*a*) correspond to the smooth surface, while those in figure 20(*b*) show the rough plate. We clearly see what the data in figure 19 indicated: the water patch grows faster with increased jet momentum on the smooth surface. However, as we examined only one rough plate, and the manual surface production may have resulted in inhomogeneities, one

https://doi.org/10.1017/jfm.2022.124 Published online by Cambridge University Press

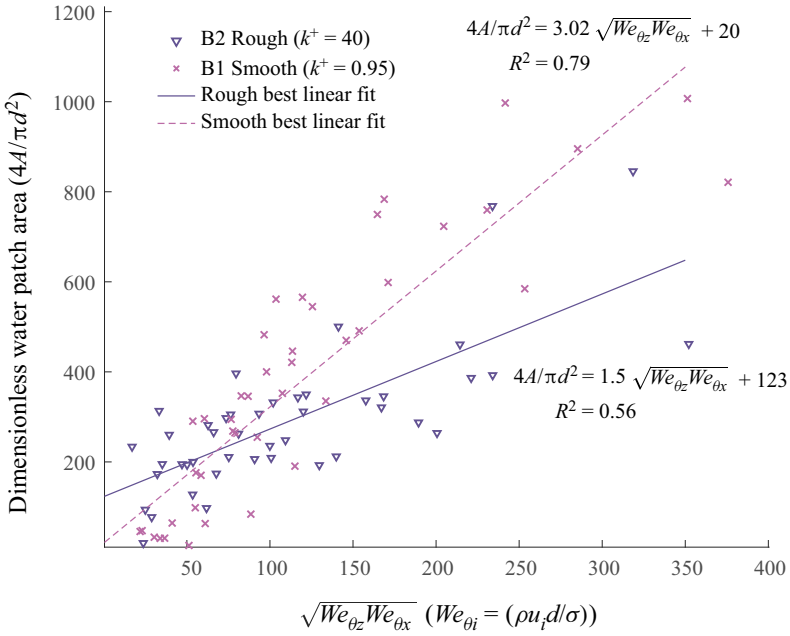

Figure 19. Water patch area on rough (B2) and smooth (B1) surfaces normalized by jet cross-section plotted against the square of the product of the contact-angle-modified Weber numbers.

should view these preliminary results with caution. To gain further insight into roughness effects, a followup study is planned.

6. Conclusions

The flow topology and horizontal force imparted by a water jet impinging on the underside of a flat plate were studied over a range of parameters. The surfaces' hydrophobicity was found to be the key parameter, and momentum loss and wetted area were found to increase with a lower surface contact angle. Regarding topology, two distinct flow behaviours were observed.

(i) For hydrophilic surfaces, both viscosity and gravity versus surface tension play dominant roles: first viscosity slows down the water until it is accumulated at the boundaries of the patch, then gravity causes droplets to fall once they grow too large (i.e. when energy is minimized by detachment).

(ii) Jet impingement on a (super)hydrophobic surface formed an ellipse shape delimited by two rims that carry the majority of the flow and enclose a laminar thin film. The interchange between kinetic energy and surface tension resembles that of a harmonic oscillator, with surface tension as the spring. The rims open up until a maximum width is reached where all lateral kinetic energy is transformed into surface energy. This is then transformed back to lateral inward kinetic energy during the second half of the water patch.

For a narrow range of parameters, reflection could occur before the rims merge, while the film remains connected to the rims and separates from the surface downstream (e.g. figure 8*b*). This could be thought of as a type of skewed water bell that appears to be rather

https://doi.org/10.1017/jfm.2022.124 Published online by Cambridge University Press

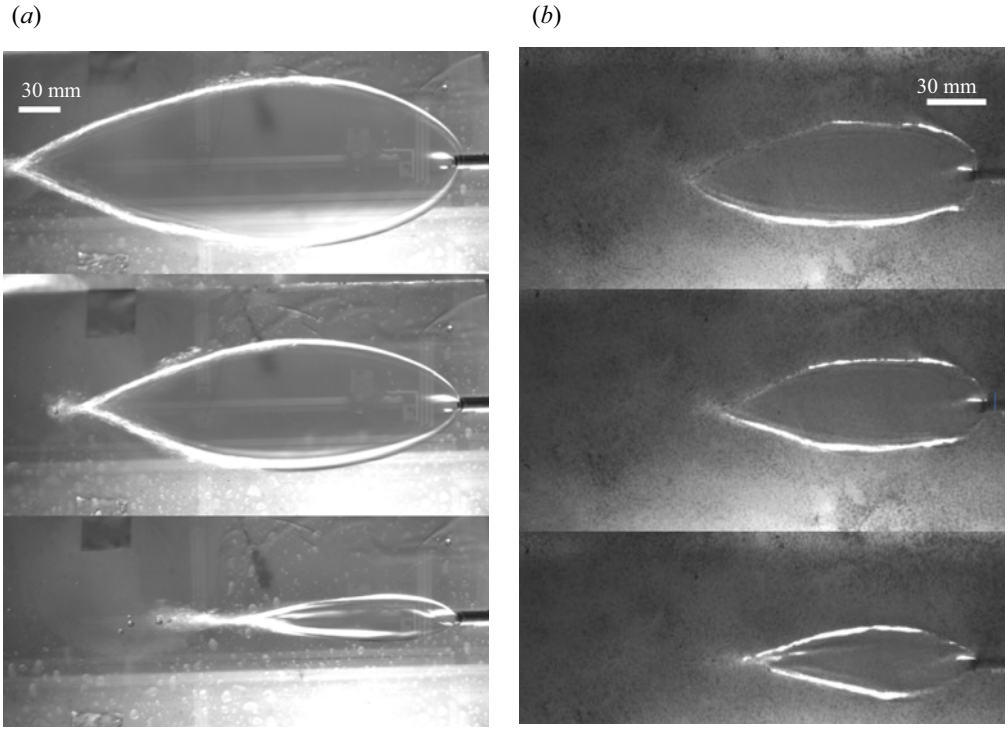

Figure 20. Top view of the water patch on (*a*) smooth surface (B1), and (*b*) rough surface (B2). From top to bottom, the flow rates are 7.71, 5.78 and 3.86 l min^{-1} ($Re = 2.01 \times 10^4$, $We = 596$; $Re = 1.51 \times 10^4$, $We = 335$; $Re = 1.01 \times 10^4$, $We = 149$). The pipe diameter (d) was 9.3 mm, and the incidence angle (α) was 25°.

unique. A simplified model for rim detachment was found to describe the observations fairly well.

Water patch width dependency on various parameters was studied and inspired the scaling with modified Weber number $We_{\theta z}$ that collapsed data. A simple model without friction aided understanding, but overpredicted patch width. A model based on Wang *et al.* (2013), which accounted for friction, provided a somewhat more satisfactory scaling, albeit it still overpredicted the width. However, this could have been expected as nothing in any of the models considered in the literature or present work accounts for the tendency of gravity to promote dewetting. This was seen particularly on the superhydrophobic surfaces, where, in an extreme case (see figure 8*b*), a 'skewed water bell' – where the film separates from the surface before the radial spread was predicted to end – was observed. An additional cause for the Wang *et al.* (2013) model's overprediction is that contrary to the momentum of the flow along a streamline at all angles ψ being balanced by the surface tension at the edges of the radial flow zone, as assumed in Wang *et al.* (2013), at maximum width, ψ is not 90° and the flow in the rims carries momentum in the streamwise direction. Hence in a future study modified boundary conditions should be explored.

The measured horizontal force, equivalent to the momentum loss of the jet, was shown to be sensitive to surface properties. While on a hydrophilic surface nominally all horizontal momentum was lost before detachment, on a hydrophobic surface the jet often detached with a significant fraction of its horizontal momentum remaining. This, along with a

https://doi.org/10.1017/jfm.2022.124 Published online by Cambridge University Press

smaller water patch area, may also in part explain observations made in context of air layer drag reduction on hydrophilic and hydrophobic surfaces Peifer *et al.* (2020) and Callahan-Dudley *et al.* (2020). These data suggest that water encountering a hydrophobic surface would be returned to the bulk flow not only sooner and after having wetted a smaller area, but also with more of its original streamwise momentum left. The latter could lessen the probability for generating another rewetting event, as the returning fluid mixes with bulk flow with nearly uniform velocity, instead of returning having lost all its momentum and hence possibly promoting overturning.

As opposed to Bush & Hasha (2004), where gravity was justifiably negligible, and by the nature of the two jets colliding there was no surface friction, the present work considered a significantly lower Froude number region. Hence it was not surprising that orientation of gravity was found to be non-negligible. Interestingly, in the present study, in some parameter ranges, the droplet ejection from the rims seen in high-speed recordings was reminiscent of 'fishbone' formation discussed in Bush & Hasha (2004). Given Re, We and $Oh(\sqrt{(We)/Re})$ the range may be also due to a Rayleigh–Plateau type instability. However, the data collected in the present study do not lend themselves to an in-depth analysis of such instabilities. Specifically, we see that compared to the flows at similar parameter ranges of Kate *et al.* (2007), Wang *et al.* (2013) and Kibar (2018), a different orientation of gravity modified the wetted patch area, force imparted and overall topology.

Data from exploratory experiments on hydraulically rough surfaces also suggest that surface roughness can significantly affect the resulting water patch area. Water spread on smooth surfaces surpassed that on rough coatings as the Weber number was increased. Further study is needed to enable a clearer explanation of the mechanisms by which roughness in conjunction with hydrophobicity effects the topology.

Finally, we may also note that a scaling of the water patch area was found with the contact-angle-modified Weber number, We_θ, which successfully predicted the fraction of wetted surface in experiments of air layer drag reduction on hydrophilic and hydrophobic surfaces (Callahan-Dudley *et al.* 2020). Despite the numerous approximations, the effect of contact angle on air layer integrity was matched qualitatively. Hence the present results begin to offer insight to a scaling that may explain data of Peifer *et al.* (2020) and Callahan-Dudley *et al.* (2020). However, further studies to enable more general quantitative prediction and consideration of roughness are needed, and such research is ongoing.

Acknowledgements. Thanks to the Justus & Louise van Effe Grant (TU Delft) for making life at Berkeley possible financially; to PhD students at UC Berkeley, K. Kadala for aiding with the contact angle measurements, and D. Grieb for helping to set up the flow loop; to C.M. Reynaud for working with R.M. during the last few months of his studies, and continuing to collect and analyse additional data during his summer visit to Berkeley; and to undergraduate students T. Streichenberger and K. Chrismanto, who helped to characterize the plates.

Funding. This research received no specific grant from any funding agency, commercial or not-for-profit sectors.

Declaration of interests. The authors report no conflict of interest.

Author ORCIDs.
Roberto M. de la Cruz https://orcid.org/0000-0001-8726-4276;
Simo A. Mäkiharju https://orcid.org/0000-0002-3818-8649.

https://doi.org/10.1017/jfm.2022.124 Published online by Cambridge University Press

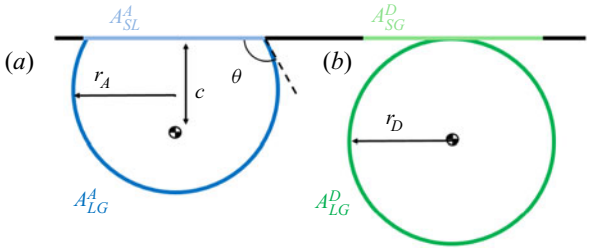

Figure 21. Rims cross-section sketch used for energy balance model for attached (*a*) versus detached (*b*) rims. Here, θ, r_A, r_D and c represent the contact angle, attached drop radius, detached drop radius and centroid distance to the surface, respectively. The A terms represent different areas per unit length according to table 6.

Variable	Attached	Detached
Area Liquid–Gas, A_{LG}	$2\theta r_A\,\Delta L$	$2\pi r_D\,\Delta L$
Area Solid–Liquid, A_{SL}	$2r_A\,\Delta L\sin\theta$	—
Area Solid–Gas[a], A_{SG}	—	$2r_A\,\Delta L\sin\theta$
Volume, V	$\dfrac{r_A^2\,\Delta L}{2}(2\theta-\sin(2\theta))$	$\pi r_D^2\,\Delta L$
Centroid, c	$r_A\left(\dfrac{4\sin^3\theta}{3(2\theta-\sin(2\theta))}-\cos\theta\right)$	r_D

Table 6. Areas and volumes per unit length, and centroids, of the attached and detached cylinder cross-sections as functions of contact angle, θ, and their radii, r_A and r_D. The two radii are related by mass conservation as $V^A = V^D$, $r_A^2 = 2\pi r_D^2/(2\theta - \sin 2\theta)$.

[a]New area of solid–gas contact created when water detaches.

Appendix A. Water detachment criteria

We consider rim detachment criteria based on an energy balance analysis with the simplifications stated below. We consider for such an analysis the two possible states of a rim at any given point of the ellipse edge, depending on the rim water volume and the surface properties.

(i) The rim remains attached to the surface. As sketched in figure 6(*c*), we assume that the rim forms a partial cylinder with a contact angle nominally equal to the static surface contact angle θ (defined in radians for definitions of table 6), and a constant volume V per unit length, ΔL, which determines the attached partial cylinder's radius, r_A.

(ii) The rim is fully detached from the surface, but is still tangent to the surface. With a radius r_D, it is taken to have a circular cross-section (figure 21).

The volume per unit length, V, contact area between solid and liquid, A_{SL}, area between liquid and gas when detached A^D_{LG}, and attached A^A_{LG}, new area created between gas and solid when water is detached, A^D_{SG}, and centroid, c, can all be computed as functions of the contact angle, θ, attached cylinder radius, r_A, and detached radius, r_D. Table 6 summarizes these values, and some are depicted in figure 21.

The question that we are trying to answer is: what is the energy associated with each of these two states, and for which surface properties and rim size is one more favourable

https://doi.org/10.1017/jfm.2022.124 Published online by Cambridge University Press

than the other? (That is, where is the limit where, energetically, it is more efficient to stay attached or detach from the surface?)

In other words, we seek to obtain the critical rim volume at which the energies of the attached and detached states are equal. Volume per unit length any larger than this critical value would lead to rim detachment. Establishing an energy balance between the two cases, assuming insignificant kinetic energy difference between the attached and detached rims states, and taking into account surface tension and gravitational potential energies, we can write

$$A^A_{LG}\sigma_{LG} + A^A_{SL}\sigma_{SL} - \rho V^A g c^A = A^D_{LG}\sigma_{LG} + A^D_{SG}\sigma_{SG} - \rho V^D g c^D, \tag{A1}$$

where the superscripts A and D indicate the attached and detached values from table 6, respectively; g is the gravitational acceleration; ρ is the water density, and σ is the surface tension between the mediums indicated with the subscripts S, L, G (solid, liquid, gas). Note the negative sign in front of the potential energy terms, as the zero potential energy line is taken at the plate height and positive upwards.

Using Young's equation to relate the surface tension forces at the triple point and the contact angle ($\sigma_{SG} - \sigma_{SL} = \sigma_{LG}\cos\theta$), and realizing that the detached solid–gas area is equal to the attached liquid–solid area ($A^D_{SG} = A^A_{SL}$), we can eliminate the unknown solid–gas and liquid–solid surface tension, replacing it by the contact angle (θ):

$$\sigma_{LG}(A^A_{LG} - A^D_{LG} - A^A_{SL}\cos\theta) - \rho g(V^A c^A - V^D c^D) = 0, \tag{A2}$$

where σ_{LG}, or just σ as defined earlier, is the air–water surface tension.

Introducing the values in table 6 into (A2) and relating the detached and attached cylinder radii by the cylinder cross-section constant volume per unit length, we find

$$r_D|_{cylinder} = f(\theta) = \sqrt{2\,\frac{\sigma}{\rho g}\,\frac{A_c(\theta)}{B_c(\theta)}}, \tag{A3}$$

where

$$A_c(\theta) = \pi + \left(\frac{2\pi}{2\theta - \sin(2\theta)}\right)^{1/2}(\sin\theta\cos\theta - \theta), \tag{A4}$$

$$B_c(\theta) = \pi - \left(\frac{2\pi^3}{2\theta - \sin(2\theta)}\right)^{1/2}\left(\frac{4\sin^3\theta}{3(2\theta - \sin(2\theta))} - \cos\theta\right). \tag{A5}$$

To consider when droplets might separate from the rims formed on the hydrophobic surfaces or from the accumulation on the edges of the patch on the hydrophilic surface A1, we repeat a similar energy analysis for droplets as discussed for cylinders above. This analysis will result in (A6) given below (and shown as a dashed line in figure 7):

$$r_D|_{droplet} = f(\theta) = \sqrt{\frac{\sigma\, A_d(\theta)}{\rho g\, B_d(\theta)}}, \tag{A6}$$

where

$$A_d(\theta) = \pi\left[(2 - 2\cos\theta)((1 - \cos\theta)(2 + \cos\theta))^{2/3} - \sin^2\theta\cos\theta\right], \tag{A7}$$

$$B_d(\theta) = \frac{\pi}{3}\left[(1 - \cos\theta)^2(2 + \cos\theta)\left(\frac{3 + 3\cos\theta}{2 + \cos\theta} - 4\cos\theta - (1-\cos\theta)^2(2+\cos\theta)\right)\right]. \tag{A8}$$

https://doi.org/10.1017/jfm.2022.124 Published online by Cambridge University Press

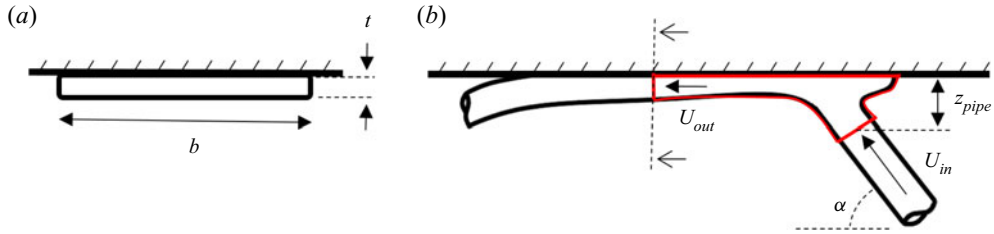

Figure 22. Sketch of control volume (red) used for derivation of a simplified model for the water patch width. Side view shown in panel (*b*), and cross-section at indicated plane in (*a*). Note that figure 6(*c*) shows a more realistic cross-section, and the rectangular approximation is adopted only for the present analysis. With this first approximation, the water patch shape is considered to be a $b \times t$ rectangle, while in actuality the cross-section consists of rims connected by a thinner film.

This predicts the size of droplets that should detach (e.g. from the hydrophilic surface A1 as water accumulates on the edges and form drops too heavy for surface tension to keep them attached). The prediction is in fair agreement with observation. Figure 8(*a*) shows detached drops from the A1 surface to be ≈6–10 mm in diameter, whereas (A6) predicted ≈8 mm to be the critical droplet diameter for detachment for surface A1.

Appendix B. Water patch width prediction

A simplified model is introduced in an attempt to better understand the dependence of the water patch maximum width on hydrophobic surfaces described in § 3.1. The approach chosen is inspired by Kaps *et al.* (2014), who asserted previously that the jet velocity x-component plays a minor role in the patch maximum width, and similarly, as a first approximation, we consider the jet's x-momentum to remain unchanged in the control volume. Mass, momentum and energy conservation are applied in the control volume shown in figure 22. The control volume begins at the jet exit from the pipe, terminating at the broadest point of the water patch on the surface. To simplify the analysis we assume the following.

(*a*) Steady state.
(*b*) Constant density, temperature and ambient pressure.
(*c*) Water loss from the rims before the location of maximum width is taken to be insignificant (i.e. water enters and exits the control volume solely via the jet and patch cross-section surfaces). Note that for the parameter range considered, this assumption was justified by observations as the modest momentum of film flow in the negative x-direction was less significant than surface tension in the $x < 0$ region. However, one should note that were the parameters to be expanded beyond the range considered, especially if the angle were to approach 90°, water loss in the negative x-direction could become significant.
(*d*) The cross-section at the widest point of the patch is approximated to be rectangular and to have a uniform velocity. (Note that figure 6(*c*) shows a more realistic cross-section that one should consider in a more detailed analysis.)
(*e*) Incoming jet velocity is nominally uniform.
(*f*) Frictional drag is neglected in the water–plate and water–air interfaces.

With the included approximations, the conservation laws for the control volume can be written as follows.

https://doi.org/10.1017/jfm.2022.124 Published online by Cambridge University Press

Conservation of mass:

With the above approximations and for convenience taking z as positive along the gravity vector, we have

$$\rho b_{max} \int_0^t u_x(y)\,\mathrm{d}z = \rho 2\pi \int_0^{d/2} u_{axial}(r)\, r\,\mathrm{d}r. \tag{B1}$$

Assuming uniform velocity at both inlet and outlet, and as by definition the measured mass flow and average jet velocity U are related by $U = 4\dot{m}/\rho\pi d^2$ and density is constant, we have

$$U_{out} b_{max} t = \pi \frac{d^2}{4} U. \tag{B2}$$

Conservation of linear momentum in x-direction:

This is given for the control volume by

$$D_{onplate} = \dot{m}_{out} U_{out} - \dot{m}_{in} \cos(\alpha)\, U, \tag{B3}$$

which, if drag were negligible and given that $\dot{m}_{in} = \dot{m}_{out}$, simplifies to

$$U_{out} = U \cos\alpha. \tag{B4}$$

Conservation of energy:

Assuming constant temperature and pressure, we consider only the surface, kinetic and potential energies, with subscripts s, k and p, respectively. We can hence write

$$\dot{E}_{s,in} + \dot{E}_{k,in} + \dot{E}_{p,in} = \dot{E}_{s,out} + \dot{E}_{k,out} + \dot{E}_{p,out}. \tag{B5}$$

Note as well that the liquid–air interface area ($A_{LG,out}$) is computed neglecting the extra interface surface from the rims' curvature and film thickness, which can be estimated to cause an approximately 2 % error. Hence, considering the simplified rectangular cross-section, we obtain

$$\begin{aligned} &\pi d U \sigma_{LG} + \tfrac{1}{2}\dot{m}_{in} U^2 + z_{pipe} g \dot{m}_{in} \\ &\quad = U_{out}[\phi\sigma_{SL} b_{max} + [(1-\phi) b_{max} + (2t + b_{max})]\sigma_{LG} - \phi\sigma_{SG} b_{max}] \\ &\qquad + \tfrac{1}{2}\dot{m}_{out} U_{out}^2 \\ &\qquad + \tfrac{1}{2}(-1) t g \dot{m}_{out}, \end{aligned} \tag{B6}$$

where σ_{LG}, σ_{SL}, σ_{SG} are the surface tensions of the liquid–air, liquid–solid and solid–air interfaces, and ϕ is the wetted fraction of the surface. Finally, note that z_{pipe} is negative.

Using Young's equation to incorporate the contact angle instead of the solid–gas and solid–liquid surface tensions, assuming $t/b_{max} \ll 1$ and reorganizing terms, gives

$$\begin{aligned} &\pi d \sigma_{LG} + \tfrac{1}{2}\rho\pi \frac{d^2}{4} U^2 + \left(z_{pipe} + \tfrac{1}{2} t\right) g \rho \pi \frac{d^2}{4} \\ &\quad = \cos(\alpha)\, b_{max} \sigma_{LG}[-\phi\cos\theta + 2 - \phi] \\ &\qquad + \tfrac{1}{2}\rho\pi \frac{d^2}{4}[\cos^2(\alpha) U^2]. \end{aligned} \tag{B7}$$

https://doi.org/10.1017/jfm.2022.124 Published online by Cambridge University Press

Finally, solving for b_{max} gives

$$\frac{b_{max}}{d} = \frac{\pi \rho d u_z^2}{8\sigma_{LG}[2-\phi(1+\cos\theta)]\cos\alpha} + \frac{\pi}{[2-\phi(1+\cos\theta)]\cos\alpha} + \frac{d\left(z_{pipe}+\frac{1}{2}t\right)g\rho\pi}{4\sigma_{LG}[2-\phi(1+\cos\theta)]\cos\alpha}. \tag{B8}$$

We note that for the (super)hydrophobic cases (A3, A4, A5), the wet fraction value is unknown, as a Cassie state may exist. However, as detailed in § 3.5, for the jet velocities used, the water in contact with the surface might be in a Wenzel state ($\phi = 1$). If the wet fraction (ϕ) is considered to be 1, meaning that all the surface in between the water and plate is wetted, and recognizing the term $\rho d u_z^2/\sigma_{GL}(1-\cos\theta)$ as the contact-angle-modified Weber number of the perpendicular jet velocity component, $We_{\theta z}$, then we find

$$\frac{b_{max}}{d}\frac{\cos\alpha}{\pi} = \frac{We_{\theta z}}{8} + \frac{1}{[1-\cos\theta]} + \frac{d\left(z_{pipe}+\frac{1}{2}t\right)g\rho}{4\sigma_{LG}[1-\cos\theta]}. \tag{B9}$$

Here,

$$\frac{d\left(z_{pipe}+\frac{1}{2}t\right)g\rho}{\sigma_{LG}[1-\cos\theta]} \tag{B10}$$

could be termed as a modified Bond (Eötvos) number Bo_{dz} as it relates the relative importance of the gravitational forces (elevation change) to surface tension:

$$\frac{b_{max}}{d}\frac{\cos\alpha}{\pi} = \frac{We_{\theta z}}{8} + \frac{1}{[1-\cos\theta]} + \frac{Bo_{dz}}{4}. \tag{B11}$$

Examining the magnitude of the modified Bond term compared to others, we find it to be always below 20 %, and below 5 % for most cases. Hence we could simplify this to

$$\frac{b_{max}}{d} = \frac{\pi}{8\cos\alpha}We_{\theta z} + \frac{\pi}{\cos\alpha[1-\cos\theta]}. \tag{B12}$$

Appendix C. Dimensional analysis

Table 2 summarizes the dimensional independent variables in this study, and ranges of their values, namely pipe diameter d, nominal jet velocity U (taken to be equal to the average velocity in the pipe), jet angle α (nominally equal to pipe angle), surface contact angle θ, surface roughness R_a, water–air surface tension σ, water dynamic viscosity μ, water density ρ, and gravity acceleration g. Flow rate would be redundant, as it can be constructed from the jet velocity and pipe diameter. These nine variables determine the output from the system, among which are the water patch area A, length L, maximum width b_{max}, and horizontal force F_x. Applying Buckingham's π theorem, four dependent groups containing the output variables above can be considered to be dependent on only six non-dimensional groups, all summarized in table 7. Additional dimensionless numbers, all

https://doi.org/10.1017/jfm.2022.124 Published online by Cambridge University Press

Parameter	Definition
Dimensionless water patch area	$4A/\pi d^2$
Dimensionless water patch length	L/d
Dimensionless water patch width	b_{max}/d
Friction coefficient	$C_F = \dfrac{F_x}{1/2\rho(U\cos(\alpha))^2 A}$
Reynolds number	$Re = \dfrac{\rho d U}{\mu}$
Weber number	$We = \dfrac{\rho d U^2}{\sigma}$
Pipe angle (deg.)	α
Contact angle (deg.)	θ
Relative roughness	$\epsilon = \dfrac{R_a}{d}$
Bond number	$Bo = \dfrac{\rho g d^2}{\sigma}$

Table 7. Set of four dependent and six independent groups resulting from the dimensional analysis. Alternative groups can be derived from these, and of particular interest in the present study is the contact-angle-modified Weber number.

derived from the ones included in table 7, and used throughout the present study, are as follows.

(i) Contact angle-modified Weber number, We_θ. This appears when analysing the energy balance of the spreading film taking into account surface tension (B12). It is therefore an expansion of the classical Weber number when surface tension effects become important, and is derived from the Weber number and the contact angle. Depending on the wetting model, different versions of this derived non-dimensional number may be relevant.

(ii) Froude number, Fr. This relates the flow inertia to the gravity, and is particularly interesting due to the connection between the present study and naval applications. It is derived from the Weber and Bond numbers as $Fr = \sqrt{We/Bo}$.

(iii) Non-dimensional roughness, k^+. The relative roughness, ϵ, gives a physical ratio between the characteristic dimension, taken as jet diameter in the present study, and physical surface roughness. However, from a general fluid dynamics point of view, it is the non-dimensional roughness, k^+, that determines if the height of the surface peaks and valleys is sufficient that they protrude through the viscous sublayer and have an influence on the flow over the surface. This is constructed as $k^+ = \rho u_\tau k_s/\mu$, where $k_s \approx 5.86\,R_a$ (Adams *et al.* 2012), and u_τ is the frictional velocity based on measured force and water patch size.

Appendix D. Raw data

Table 8 shows the data in raw format to facilitate further comparison to theory and other experiments. Uncertainties based on instrumentation or standard deviation of a number of measurements were below 0.1 mm for pipe diameter d, 1.5° for pipe angle α, 0.08 l min^{-1} for flow rate Q, 8° for the contact angle θ, 4 mm for the length L and maximum width b_{max} of the ellipse, and 0.003 N for the horizontal force F_x.

https://doi.org/10.1017/jfm.2022.124 Published online by Cambridge University Press

d (mm)	α (deg.)	Q ($\mathrm{l\,min^{-1}}$)	θ (deg.)	Re ($\times 10^3$)	We	We_θ	$We_{\theta x}$	$We_{\theta z}$	Bo	Fr	F_x (N)	L (mm)	b_{max} (mm)
6.1	15	3.06	150	12.2	270	144	135	10	5.1	7.3	0.000	97	15
6.1	15	3.79	150	15.2	414	222	207	15	5.1	9.0	0.046	151	22
6.1	30	2.18	150	8.7	137	73	55	18	5.1	5.2	0.004	92	30
6.1	15	3.08	150	12.3	273	146	137	10	5.1	7.3	0.054	224	35
6.1	55	2.51	150	10.0	181	97	32	65	5.1	6.0	0.008	97	60
6.1	30	4.36	150	17.5	549	294	221	74	5.1	10.4	0.071	192	75
6.1	55	3.28	150	13.1	310	166	55	112	5.1	7.8	0.025	124	86
6.1	30	5.58	150	22.3	897	481	361	120	5.1	13.3	0.162	230	97
6.1	55	4.53	150	18.2	593	318	104	213	5.1	10.8	0.074	166	114
9.2	15	7.34	150	19.6	460	246	230	16	11.5	6.3	0.019	218	33
9.2	30.5	4.16	150	11.1	148	79	59	20	11.5	3.6	0.056	103	29
9.2	15	8.52	150	22.7	619	332	310	22	11.5	7.3	0.021	272	41
9.2	15	9.74	150	26.0	809	434	405	29	11.5	8.4	0.058	321	52
9.2	30.5	5.63	150	15.0	270	145	107	37	11.5	4.8	0.016	191	67
9.2	55	3.53	150	9.4	106	57	19	38	11.5	3.0	0.006	94	55
9.2	30.5	7.32	150	19.5	457	245	182	63	11.5	6.3	0.070	237	80
9.2	55	5.10	150	13.6	222	119	39	80	11.5	4.4	0.023	160	103
9.2	55	6.26	150	16.7	334	179	59	120	11.5	5.4	0.047	204	131
9.2	55	8.82	150	23.5	664	356	117	239	11.5	7.6	0.122	191	159
14.0	30	7.65	150	13.4	142	76	57	19	26.7	2.3	0.035	133	29
14.0	54.5	5.13	150	9.0	64	34	12	23	26.7	1.5	0.000	77	45
14.0	30	10.79	150	18.9	282	151	113	38	26.7	3.3	0.008	240	72
14.0	54.5	7.49	150	13.1	136	73	25	48	26.7	2.3	0.045	169	93
14.0	30	12.92	150	22.7	405	217	163	54	26.7	3.9	0.039	309	101
4.7	35	1.96	150	10.2	243	130	87	43	3.0	8.9	0.054	92	35
4.7	35	2.63	150	13.7	437	234	157	77	3.0	12.0	0.045	120	55
4.7	45	1.85	150	9.6	217	116	58	58	3.0	8.5	0.014	81	39
4.7	45	0.89	150	4.6	50	27	13	13	3.0	4.1	0.003	34	49
14.0	54.5	10.61	150	18.6	273	146	49	97	26.7	3.2	0.059	302	187
4.7	25	1.21	150	6.3	93	50	41	9	3.0	5.5	0.020	30	10
4.7	25	2.46	150	12.8	382	205	168	37	3.0	11.2	0.020	113	29
4.7	25	3.45	150	17.9	750	402	330	72	3.0	15.7	0.091	165	47
4.7	25	4.74	150	24.7	1421	762	626	136	3.0	21.7	0.224	213	60
4.7	35	0.87	150	4.5	48	26	17	8	3.0	4.0	0.001	34	13
4.7	35	1.85	150	9.6	217	116	78	38	3.0	8.5	0.011	90	38
4.7	35	2.66	150	13.8	447	239	161	79	3.0	12.1	0.045	123	52
4.7	35	3.56	150	18.5	799	428	287	141	3.0	16.2	0.105	145	65
4.7	45	1.43	150	7.4	129	69	35	35	3.0	6.5	0.005	60	32
4.7	45	2.25	150	11.7	321	172	86	86	3.0	10.3	0.030	96	56
4.7	45	2.94	150	15.3	548	294	147	147	3.0	13.4	0.066	97	70
4.7	45	0.75	150	3.9	36	19	10	10	3.0	3.4	0.000	31	15
6.1	35	3.01	150	12.0	261	140	94	46	5.1	7.1	0.019	131	54
6.1	25	2.43	150	9.7	171	91	75	16	5.1	5.8	0.005	78	23
6.1	25	3.29	150	13.2	313	168	138	30	5.1	7.8	0.017	123	38
6.1	25	4.52	150	18.1	588	315	259	56	5.1	10.7	0.069	174	55
6.1	25	6.10	150	24.4	1072	574	472	103	5.1	14.5	0.183	232	70
6.1	35	1.52	150	6.1	66	36	24	12	5.1	3.6	0.001	46	18
6.1	35	4.37	150	17.5	550	295	198	97	5.1	10.4	0.073	148	83
6.1	35	5.81	150	23.3	975	522	350	172	5.1	13.8	0.167	176	93
6.1	45	1.19	150	4.8	41	22	11	11	5.1	2.8	0.001	37	16
6.1	45	2.43	150	9.7	170	91	46	46	5.1	5.8	0.011	82	45
6.1	45	3.70	150	14.8	394	211	106	106	5.1	8.8	0.043	136	81
6.1	45	4.78	150	19.1	658	353	176	176	5.1	11.3	0.086	118	100

Table 8. For caption see next page.

https://doi.org/10.1017/jfm.2022.124 Published online by Cambridge University Press

d (mm)	α (deg.)	Q ($\mathrm{l\,min^{-1}}$)	θ (deg.)	Re ($\times 10^3$)	We	We_θ	$We_{\theta x}$	$We_{\theta z}$	Bo	Fr	F_x (N)	L (mm)	b_{max} (mm)
9.3	25	7.69	150	20.3	489	262	215	47	11.8	6.4	0.054	211	79
9.3	25	3.84	150	10.1	122	65	53	12	11.8	3.2	0.001	47	17
9.3	25	5.83	150	15.4	280	150	123	27	11.8	4.9	0.009	117	45
9.3	35	8.53	150	22.5	601	322	216	106	11.8	7.2	0.114	180	125
9.3	35	2.14	150	5.7	38	20	14	7	11.8	1.8	0.002	25	13
9.3	35	4.28	150	11.3	152	81	55	27	11.8	3.6	0.006	84	52
9.3	35	6.24	150	16.5	321	172	116	57	11.8	5.2	0.039	164	84
9.3	45	9.36	150	24.7	724	388	194	194	11.8	7.8	0.143	176	155
9.3	45	2.88	150	7.6	69	37	18	18	11.8	2.4	0.001	43	36
9.3	45	4.76	150	12.6	187	100	50	50	11.8	4.0	0.017	124	77
9.3	45	6.88	150	18.2	391	209	105	105	11.8	5.8	0.063	166	122
14.0	30	10.53	45	18.5	268	916	687	229	26.7	3.2	0.121	461	239
14.0	30	7.91	45	13.9	152	518	388	129	26.7	2.4	0.045	338	144
14.0	54.5	7.56	45	13.3	138	472	159	313	26.7	2.3	0.069	393	307
14.0	54.5	9.46	45	16.6	217	740	249	490	26.7	2.9	0.123	420	333
14.0	54.5	4.86	45	8.5	57	195	66	129	26.7	1.5	0.017	247	183
6.1	15	1.78	45	7.1	91	311	290	21	5.1	4.2	0.019	381	60
6.1	15	1.41	45	5.6	57	195	182	13	5.1	3.3	0.012	299	66
6.1	15	2.28	45	9.1	150	511	477	34	5.1	5.4	0.039	382	120
6.1	30	1.76	45	7.1	89	305	229	76	5.1	4.2	0.021	234	150
6.1	30	2.27	45	9.1	149	507	380	127	5.1	5.4	0.038	304	156
6.1	30	3.07	45	12.3	271	925	694	231	5.1	7.3	0.071	343	177
6.1	55	2.25	45	9.0	147	501	165	336	5.1	5.4	0.027	215	183
6.1	55	3.05	45	12.2	268	917	302	615	5.1	7.2	0.051	294	250
6.1	55	3.81	45	15.2	418	1427	469	957	5.1	9.0	0.084	332	282
9.2	15	3.71	45	9.9	117	401	374	27	11.5	3.2	0.004	156	37
9.2	15	4.98	45	13.3	212	723	674	48	11.5	4.3	0.035	300	92
9.2	15	5.41	45	14.4	250	854	796	57	11.5	4.7	0.056	345	118
9.2	30	2.89	45	7.7	71	244	183	61	11.5	2.5	0.038	183	72
9.2	30	3.70	45	9.9	117	399	300	100	11.5	3.2	0.029	312	144
9.2	30	4.72	45	12.6	190	649	486	162	11.5	4.1	0.064	391	222
9.2	55	3.69	45	9.9	116	398	131	267	11.5	3.2	0.027	302	264
9.2	55	4.98	45	13.3	211	721	237	484	11.5	4.3	0.052	341	299
9.3	35	2.35	45	6.2	45	155	104	51	11.8	2.0	0.016	50	30
9.3	35	3.55	45	9.4	104	355	238	117	11.8	3.0	0.023	337	210
9.3	45	2.32	45	6.1	44	152	76	76	11.8	1.9	0.012	146	87
9.3	35	4.36	45	11.5	157	536	360	176	11.8	3.7	0.045	286	172
9.2	55	6.19	45	16.5	327	1118	368	750	11.5	5.3	0.083	389	341
9.3	25	3.11	45	8.2	80	273	224	49	11.8	2.6	0.011	269	93
9.3	25	4.28	45	11.3	152	517	425	92	11.8	3.6	0.054	414	174
9.3	35	2.12	45	5.6	37	127	85	42	11.8	1.8	0.006	229	76
9.3	35	3.11	45	8.2	80	273	183	90	11.8	2.6	0.031	337	210
9.3	35	4.29	45	11.3	152	518	348	170	11.8	3.6	0.057	392	209
9.3	45	2.36	45	6.2	46	157	78	78	11.8	2.0	0.015	275	141
9.3	45	3.58	45	9.5	106	362	181	181	11.8	3.0	0.035	333	180
9.3	45	4.75	45	12.5	186	637	318	318	11.8	4.0	0.065	362	297
4.7	35	2.15	45	11.2	292	998	669	328	3.0	9.8	0.065	294	186
4.7	25	1.95	45	10.1	240	819	673	146	3.0	8.9	0.056	325	137
4.7	25	3.25	45	16.9	667	2276	1869	406	3.0	14.8	0.152	365	175
4.7	35	1.48	45	7.7	139	473	317	156	3.0	6.8	0.031	256	152
4.7	35	2.55	45	13.2	410	1398	938	460	3.0	11.6	0.089	318	196
4.7	45	1.48	45	7.7	139	474	237	237	3.0	6.8	0.028	226	162
4.7	45	2.15	45	11.2	291	995	497	497	3.0	9.8	0.058	261	172
4.7	45	2.90	45	15.1	531	1814	907	907	3.0	13.2	0.103	304	211

Table 8. For caption see next page.

https://doi.org/10.1017/jfm.2022.124 Published online by Cambridge University Press

d (mm)	α (deg.)	Q ($\mathrm{l\,min^{-1}}$)	θ (deg.)	Re ($\times 10^3$)	We	We_θ	$We_{\theta x}$	$We_{\theta z}$	Bo	Fr	F_x (N)	L (mm)	b_{max} (mm)
6.1	25	1.36	45	5.4	53	181	149	32	5.1	3.2	0.013	276	79
6.1	25	1.99	45	8.0	114	390	320	70	5.1	4.7	0.032	303	139
6.1	35	1.18	45	4.7	40	137	92	45	5.1	2.8	0.011	193	91
6.1	35	1.99	45	8.0	114	390	262	128	5.1	4.7	0.031	267	162
6.1	35	2.59	45	10.4	193	658	442	217	5.1	6.1	0.053	308	179
6.1	45	1.01	45	4.0	29	100	50	50	5.1	2.4	0.009	167	101
6.1	45	2.15	45	8.6	133	453	227	227	5.1	5.1	0.034	273	179
6.1	45	2.87	45	11.5	238	812	406	406	5.1	6.8	0.058	303	207
4.7	25	1.21	142	6.3	92	51	42	9	3.0	5.5	0.003	48	13
4.7	25	2.45	142	12.7	380	212	174	38	3.0	11.2	0.049	125	35
4.7	25	3.45	142	17.9	751	420	345	75	3.0	15.7	0.126	159	49
4.7	25	4.74	142	24.6	1418	793	651	142	3.0	21.6	0.262	188	70
4.7	35	0.86	142	4.5	47	26	18	9	3.0	3.9	0.001	38	13
4.7	35	1.85	142	9.6	215	120	81	40	3.0	8.4	0.022	94	38
4.7	35	2.65	142	13.8	443	248	166	82	3.0	12.1	0.066	129	59
4.7	35	3.54	142	18.4	794	444	298	146	3.0	16.2	0.137	144	72
4.7	45	1.43	142	7.4	129	72	36	36	3.0	6.5	0.010	69	36
4.7	45	2.25	142	11.7	321	180	90	90	3.0	10.3	0.039	83	58
4.7	45	2.95	142	15.4	551	308	154	154	3.0	13.5	0.081	114	75
4.7	45	0.75	142	3.9	35	20	10	10	3.0	3.4	0.003	21	13
6.1	25	2.42	142	9.7	169	95	78	17	5.1	5.8	0.007	75	21
6.1	25	3.29	142	13.2	312	175	143	31	5.1	7.8	0.039	122	39
6.1	25	4.53	142	18.2	593	332	272	59	5.1	10.8	0.111	172	61
6.1	25	6.12	142	24.5	1081	605	497	108	5.1	14.5	0.233	232	81
6.1	35	1.53	142	6.1	68	38	25	12	5.1	3.6	0.002	35	18
6.1	35	3.02	142	12.1	263	147	99	48	5.1	7.2	0.029	125	49
6.1	35	4.41	142	17.7	561	314	211	103	5.1	10.5	0.105	176	84
6.1	35	5.87	142	23.5	994	556	373	183	5.1	13.9	0.215	201	100
6.1	45	1.20	142	4.8	42	23	12	12	5.1	2.9	−0.004	25	19
6.1	45	2.44	142	9.8	172	96	48	48	5.1	5.8	0.016	89	49
6.1	45	3.71	142	14.9	397	222	111	111	5.1	8.8	0.063	134	85
6.1	45	4.80	142	19.2	665	372	186	186	5.1	11.4	0.125	160	105
9.3	25	7.71	142	20.4	491	275	226	49	11.8	6.5	0.090	213	71
9.3	25	3.84	142	10.1	122	68	56	12	11.8	3.2	0.001	48	17
9.3	25	5.82	142	15.4	280	157	129	28	11.8	4.9	0.020	140	45
9.3	35	8.55	142	22.6	604	338	227	111	11.8	7.2	0.153	257	117
9.3	35	2.14	142	5.6	38	21	14	7	11.8	1.8	0.000	16	14
9.3	35	4.30	142	11.4	153	86	57	28	11.8	3.6	0.009	92	48
9.3	35	6.26	142	16.5	324	181	122	60	11.8	5.2	0.054	178	86
9.3	45	9.32	142	24.6	718	401	201	201	11.8	7.8	0.206	238	156
9.3	45	2.86	142	7.6	68	38	19	19	11.8	2.4	0.002	67	35
9.3	45	4.74	142	12.5	186	104	52	52	11.8	4.0	0.022	145	79
9.3	45	6.85	142	18.1	388	217	108	108	11.8	5.7	0.095	179	124
14.0	15	13.64	101	23.9	451	379	353	25	26.7	4.1	0.063	254	60
14.0	30	7.64	101	13.4	141	119	89	30	26.7	2.3	0.028	127	49
14.0	30	10.81	101	19.0	283	238	178	59	26.7	3.3	0.078	313	110
14.0	30	12.92	101	23.9	451	379	284	95	26.7	4.1	0.155	438	143
14.0	54.5	10.03	101	17.6	243	204	69	135	26.7	3.0	0.070	341	232
14.0	54.5	4.87	101	8.5	58	48	16	32	26.7	1.5	0.004	114	77
14.0	54.5	7.50	101	13.2	136	115	39	76	26.7	2.3	0.021	268	146
6.1	15	2.76	101	11.1	220	185	173	12	5.1	6.6	0.017	147	21
6.1	15	4.00	101	16.0	461	387	361	26	5.1	9.5	0.078	261	44
6.1	15	6.08	101	24.3	1065	894	834	60	5.1	14.4	0.264	365	79
6.1	30	2.60	101	10.4	195	163	123	41	5.1	6.2	0.027	181	50
6.1	30	3.53	101	14.2	360	302	227	76	5.1	8.4	0.074	237	76

Table 8. For caption see next page.

https://doi.org/10.1017/jfm.2022.124 Published online by Cambridge University Press

d (mm)	α (deg.)	Q ($\mathrm{l\,min^{-1}}$)	θ (deg.)	Re ($\times 10^3$)	We	We_θ	$We_{\theta x}$	$We_{\theta z}$	Bo	Fr	F_x (N)	L (mm)	b_{max} (mm)
6.1	30	5.04	101	20.2	733	615	462	154	5.1	12.0	0.179	292	98
6.1	55	2.28	101	9.1	150	126	41	85	5.1	5.4	0.021	123	80
6.1	55	3.70	101	14.8	395	332	109	223	5.1	8.8	0.066	175	135
9.2	15	7.02	101	18.7	421	353	330	24	11.5	6.0	0.112	372	74
9.2	15	5.97	101	15.9	304	255	238	17	11.5	5.1	0.020	219	38
9.2	15	7.27	101	19.4	451	379	354	25	11.5	6.3	0.069	318	61
9.2	30	8.64	101	23.1	637	535	401	134	11.5	7.4	0.214	365	160
9.2	30	3.44	101	9.2	101	85	64	21	11.5	3.0	0.007	125	35
9.2	30	6.20	101	16.5	328	275	206	69	11.5	5.3	0.091	277	127
9.2	55	9.60	101	25.6	787	661	217	443	11.5	8.3	0.179	354	246
9.2	55	4.23	101	11.3	153	128	42	86	11.5	3.6	0.018	178	107
4.7	25	5.03	101	26.2	1601	1345	1105	240	3.0	23.0	0.332	291	97
4.7	45	2.26	101	11.8	324	272	136	136	3.0	10.3	0.050	136	78
4.7	45	3.03	101	15.8	581	488	244	244	3.0	13.8	0.095	170	99
6.1	25	5.24	101	21.0	793	666	547	119	5.1	12.5	0.191	249	79
6.1	25	6.30	101	25.2	1146	962	790	172	5.1	15.0	0.281	302	99
6.1	45	4.02	101	16.1	467	392	196	196	5.1	9.6	0.092	170	113
6.1	45	5.16	101	20.7	768	645	323	323	5.1	12.3	0.157	223	134
9.2	55	7.21	101	19.2	443	372	122	250	11.5	6.2	0.081	291	196
4.7	25	1.18	101	6.1	88	74	61	13	3.0	5.4	0.004	81	12
4.7	25	3.41	101	17.7	734	616	506	110	3.0	15.6	0.146	227	72
4.7	25	4.70	101	24.4	1393	1170	961	209	3.0	21.4	0.293	291	97
4.7	35	0.82	101	4.3	43	36	24	12	3.0	3.8	0.003	65	19
4.7	35	1.79	101	9.3	203	170	114	56	3.0	8.2	0.033	130	53
4.7	25	2.41	101	12.5	367	308	253	55	3.0	11.0	0.064	186	51
9.3	35	8.28	101	21.9	567	476	319	157	11.8	6.9	0.181	322	154
9.3	45	9.13	101	24.1	689	578	289	289	11.8	7.7	0.215	322	180
9.3	45	2.78	101	7.3	64	54	27	27	11.8	2.3	0.007	96	48
9.3	45	4.58	101	12.1	173	145	73	73	11.8	3.8	0.038	207	103
9.3	45	6.64	101	17.5	364	306	153	153	11.8	5.6	0.104	250	152
4.7	35	3.50	101	18.2	774	650	436	214	3.0	16.0	0.150	207	103
4.7	45	2.18	101	11.3	299	251	126	126	3.0	9.9	0.048	138	80
4.7	35	2.59	101	13.5	423	355	238	117	3.0	11.8	0.077	171	77
4.7	45	1.45	101	7.6	133	112	56	56	3.0	6.6	0.027	121	57
4.7	45	2.18	101	11.3	299	251	126	126	3.0	9.9	0.049	136	78
4.7	45	2.87	101	14.9	520	436	218	218	3.0	13.1	0.089	170	99
4.7	45	0.70	101	3.7	31	26	13	13	3.0	3.2	0.008	41	20
6.1	25	2.40	101	9.6	166	140	115	25	5.1	5.7	0.017	141	28
6.1	25	3.24	101	13.0	303	255	209	45	5.1	7.7	0.056	199	50
6.1	25	4.47	101	17.9	576	484	397	86	5.1	10.6	0.134	249	79
6.1	25	6.06	101	24.3	1060	890	731	159	5.1	14.4	0.264	302	99
6.1	35	1.41	101	5.6	57	48	32	16	5.1	3.4	0.011	75	25
6.1	35	2.89	101	11.6	241	203	136	67	5.1	6.9	0.047	178	72
6.1	35	4.32	101	17.3	539	453	304	149	5.1	10.3	0.123	237	108
6.1	35	4.99	101	20.0	719	604	405	199	5.1	11.9	0.169	241	117
6.1	35	5.79	101	23.2	968	813	545	267	5.1	13.8	0.232	280	129
6.1	45	1.06	101	4.2	32	27	14	14	5.1	2.5	0.002	49	25
6.1	45	2.31	101	9.2	154	129	65	65	5.1	5.5	0.028	135	84
6.1	45	3.56	101	14.2	365	306	153	153	5.1	8.4	0.074	170	113
9.3	35	6.03	101	15.9	300	252	169	83	11.8	5.0	0.084	238	122
6.1	45	4.64	101	18.6	620	521	260	260	5.1	11.0	0.133	151	135
9.3	25	7.52	101	19.9	467	393	322	70	11.8	6.3	0.145	328	117
9.3	25	3.70	101	9.8	113	95	78	17	11.8	3.1	0.007	110	29
9.3	25	5.65	101	14.9	264	222	182	40	11.8	4.7	0.059	254	72
9.3	35	2.07	101	5.5	35	30	20	10	11.8	1.7	0.003	34	15
9.3	35	4.13	101	10.9	141	118	79	39	11.8	3.5	0.023	170	64

Table 8. Raw data for the superhydrohphobic 'A' surfaces.

https://doi.org/10.1017/jfm.2022.124 Published online by Cambridge University Press

References

Adams, T., Grant, C. & Watson, H. 2012 A simple algorithm to relate measured surface roughness to equivalent sand-grain roughness. *Intl J. Mech. Engng Mechatron.* **1** (2), 66–71.

Bhagat, R.K., Jha, N.K., Linden, P.F. & Wilson, D.I. 2018 On the origin of the circular hydraulic jump in a thin liquid film. *J. Fluid Mech.* **851**, R5.

Bhagat, R.K. & Linden, P.F. 2020 The circular capillary jump. *J. Fluid Mech.* **896**, A25.

Brunet, P., Clanet, C. & Limat, L. 2004 Transonic liquid bells. *Phys. Fluids* **16** (7), 2668–2678.

Bush, J.W.M. & Hasha, A.E. 2004 On the collision of laminar jets: fluid chains and fishbones. *J. Fluid Mech.* **511**, 285.

Button, E.C., Davidson, J.F., Jameson, G.J. & Sader, J.E. 2010 Water bells formed on the underside of a horizontal plate. Part 2. Theory. *J. Fluid Mech.* **649**, 45–68.

Callahan-Dudley, C., Tecson, C., Martinez de la Cruz, R. & Mäkiharju, S.A. 2020 Superhydrophobic surface air layer drag reduction. In *Proc. 33rd Symposium on Naval Hydrodynamics, Osaka, Japan*.

Ceccio, S.L. 2010 Friction drag reduction of external flows with bubble and gas injection. *Annu. Rev. Fluid Mech.* **42** (1), 183–203.

Celestini, F., Kofman, R., Noblin, X. & Pellegrin, M. 2010 Water jet rebounds on hydrophobic surfaces: a first step to jet micro-fluidics. *Soft Matt.* **6** (23), 5872–5876.

Cencel, Y.A. & Cimbala, J.M. 2006 *Fluid Mechanics – Fundamentals and Applications*. McGraw-Hill Internat. Ed.

Daerr, A. & Mogne, A. 2016 Pendent_drop: an imagej plugin to measure the surface tension from an image of a pendent drop. *J. Open Res. Softw.* **4** (1), p.e3.

Duchesne, A., Andersen, A. & Bohr, T. 2019 Surface tension and the origin of the circular hydraulic jump in a thin liquid film. *Phys. Rev. Fluids* **4** (8), 084001.

Elbing, B.R., Mäkiharju, S., Wiggins, A., Perlin, M., Dowling, D.R. & Ceccio, S.L. 2013 On the scaling of air layer drag reduction. *J. Fluid Mech.* **717**, 484–513.

Gose, J.W., Golovin, K., Boban, M., Mabry, J.M., Tuteja, A., Perlin, M. & Ceccio, S.L. 2018 Characterization of superhydrophobic surfaces for drag reduction in turbulent flow. *J. Fluid Mech.* **845**, 560–580.

Jameson, G.J., Jenkins, C.E., Button, E.C. & Sader, J.E. 2010 Water bells formed on the underside of a horizontal plate. Part 1. Experimental investigation. *J. Fluid Mech.* **649**, 19–43.

Kaps, S., Adelung, R., Scharnberg, M., Faupel, F., Milenkovic, S. & Hassel, A.W. 2014 Determining superhydrophobic surfaces from an expanded Cassie–Baxter equation describing simple wettability experiments. arXiv:1408.5273.

Kate, R.P., Das, P.K. & Chakraborty, S. 2007 Hydraulic jumps due to oblique impingement of circular liquid jets on a flat horizontal surface. *J. Fluid Mech.* **573**, 247–263.

Kibar, A. 2015 Experimental and numerical investigations of the impingement of an oblique liquid jet onto a superhydrophobic surface: energy transformation. *Fluid Dyn. Res.* **48** (1), 015501.

Kibar, A. 2018 Experimental and numerical investigation on a liquid jet impinging on a vertical superhydrophobic surface: spreading and reflection. *Prog. Comput. Fluid Dyn. Intl J.* **18** (3), 150–163.

Kibar, A., Karabay, H., Yiğit, K.S., Ucar, I.O. & Erbil, H.Y. 2010 Experimental investigation of inclined liquid water jet flow onto vertically located superhydrophobic surfaces. *Exp. Fluids* **49** (5), 1135–1145.

Kibar, A. & Yiğit, K.S. 2018 The spreading profile of an impinging liquid jet on the hydrophobic surfaces. *Sigma* **36** (3), 609–618.

Kim, D. & Moin, P. 2010 Direct numerical study of air layer drag reduction phenomenon over a backward-facing step. *Center Turbul. Res. Annu. Res. Briefs*, 351–363.

Lapham, G.S., Dowling, D.R. & Schultz, W.W. 1999 In situ force-balance tensiometry. *Exp. Fluids* **27** (2), 157–166.

Mäkiharju, S.A. & Ceccio, S.L. 2018 On multi-point gas injection to form an air layer for frictional drag reduction. *Ocean Engng* **147**, 206–214.

Mäkiharju, S.A., Lee, I.-H.R., Filip, G.P., Maki, K.J. & Ceccio, S.L. 2017 The topology of gas jets injected beneath a surface and subject to liquid cross-flow. *J. Fluid Mech.* **818**, 141–183.

Mäkiharju, S.A., Perlin, M. & Ceccio, S.L. 2012 On the energy economics of air lubrication drag reduction. *Intl J. Nav. Archit. Ocean Engng* **4** (4), 412–422.

Manik, J., Dalal, A. & Natarajan, G. 2019 A parametric study on the droplet detachment process from the ceiling under the effect of gravity. *Engng Comput.* **36** (2), 445–465.

Mertens, K., Putkaradze, V. & Vorobieff, P. 2005 Morphology of a stream flowing down an inclined plane. Part 1. Braiding. *J. Fluid Mech.* **531**, 49–58.

https://doi.org/10.1017/jfm.2022.124 Published online by Cambridge University Press

MOITRA, S., ROY, T., GANGULY, R. & MEGARIDIS, C.M. 2021 Jet impact on superhydrophobic metal mesh. *Langmuir* **37** (9), 2891–2899.

PEIFER, B.C., CALLAHAN-DUDLEY, C. & MÄKIHARJU, S.A. 2020 Air layer on superhydrophobic surface for frictional drag reduction. *J. Ship Res.* **64** (2), 118–126.

PRINCE, J.F., MAYNES, D. & CROCKETT, J. 2015 On jet impingement and thin film breakup on a horizontal superhydrophobic surface. *Phys. Fluids* **27** (11), 112108.

SANDERS, W.C., WINKEL, E.S., DOWLING, D.R., PERLIN, M. & CECCIO, S.L. 2006 Bubble friction drag reduction in a high-Reynolds-number flat-plate turbulent boundary layer. *J. Fluid Mech.* **552**, 353–380.

SON, Y. & KIM, C. 2009 Spreading of inkjet droplet of non-Newtonian fluid on solid surface with controlled contact angle at low Weber and Reynolds numbers. *J. Non-Newtonian Fluid Mech.* **162** (1–3), 78–87.

WANG, T., FARIA, D., STEVENS, L.J., TAN, J.S.C., DAVIDSON, J.F. & WILSON, D.I. 2013 Flow patterns and draining films created by horizontal and inclined coherent water jets impinging on vertical walls. *Chem. Engng Sci.* **102**, 585–601.

WATSON, E.J. 1964 The radial spread of a liquid jet over a horizontal plane. *J. Fluid Mech.* **20** (3), 481–499.

WILSON, D.I., LE, B.L., DAO, H.D.A., LAI, K.Y., MORISON, K.R. & DAVIDSON, J.F. 2012 Surface flow and drainage films created by horizontal impinging liquid jets. *Chem. Engng Sci.* **68** (1), 449–460.

ZHENG, Q.-S., YU, Y. & ZHAO, Z.-H. 2005 Effects of hydraulic pressure on the stability and transition of wetting modes of superhydrophobic surfaces. *Langmuir* **21** (26), 12207–12212.

https://doi.org/10.1017/jfm.2022.124 Published online by Cambridge University Press